The "Giraffe": Discovery of a $2-3\ M_\odot$ dark companion to a stripped red giant

T. Jayasinghe[1,2]★, Todd A. Thompson[1,2], C. S. Kochanek[1,2], K. Z. Stanek[1,2], D. M. Rowan[1,2], D. V. Martin[1,3,2], P. J. Vallely[1,2], J. T. Hinkle[4], D. Huber[4], H. Isaacson[5,6], J. Tayar[4,7], K. Auchettl[8,9,10], I. Ilyin[11], A. W. Howard[12], C. Badenes[13]

[1]*Department of Astronomy, The Ohio State University, 140 West 18th Avenue, Columbus, OH 43210, USA*
[2]*Center for Cosmology and Astroparticle Physics, The Ohio State University, 191 W. Woodruff Avenue, Columbus, OH 43210, USA*
[3]*NASA Sagan Fellow*
[4]*Institute for Astronomy, University of Hawai'i, 2680 Woodlawn Drive, Honolulu, HI 96822, USA*
[5]*Department of Astronomy, University of California Berkeley, Berkeley CA 94720, USA*
[6]*Centre for Astrophysics, University of Southern Queensland, Toowoomba, QLD, Australia*
[7]*Department of Astronomy, University of Florida, Bryant Space Science Center, Stadium Road, Gainesville, FL 32611, USA*
[8]*OzGrav, School of Physics, The University of Melbourne, Parkville, Victoria 3010, Australia*
[9]*ARC Centre of Excellence for All Sky Astrophysics in 3 Dimensions (ASTRO 3D)*
[10]*Department of Astronomy and Astrophysics, University of California, Santa Cruz, CA 95064, USA*
[11]*Leibniz Institute for Astrophysics Potsdam (AIP), An der Sternwarte 16, D-14482 Potsdam, Germany*
[12]*Department of Astronomy, California Institute of Technology, Pasadena, CA 91125, USA*
[13]*Department of Physics and Astronomy and Pittsburgh Particle Physics, Astrophysics and Cosmology Center (PITT PACC), University of Pittsburgh, 3941 O'Hara Street, Pittsburgh, PA 15260, USA*

Accepted XXX. Received YYY; in original form ZZZ

ABSTRACT

We report the discovery of a massive $\sim 2-3\ M_\odot$ object as a binary companion to 2M04123153+6738486 (2M0412). 2M0412 is an evolved ($T_{\rm eff,giant} \simeq 4200$ K), luminous ($L_{\rm giant} \simeq 230\ L_\odot$) red giant in a circular $P = 81.2$ d binary. 2M0412 is a known variable star previously classified as a semi-regular variable. The ASAS-SN, ATLAS, *TESS* and ZTF light curves show that the giant is a nearly Roche lobe filling ellipsoidal variable with an inclination of $41.9° \pm 0.1°$, a mass ratio of $q \simeq 0.20 \pm 0.01$, a companion mass of $M_{\rm comp} = 2.97 \pm 0.02\ M_\odot$, and a giant mass of $M_{\rm giant} = 0.60 \pm 0.01\ M_\odot$ for a distance of $\simeq 4$ kpc. The mass of the giant indicates that its envelope is stripped. The cross-correlation functions of the Keck/HIRES and LBT/PEPSI spectra show a second RV signal implying a consistent mass ratio of $q \simeq 0.20 \pm 0.01$. We also identify an orbital phase dependent, broad Hα emission line. The simplest explanation for the massive companion is a single mass-gap black hole or a high mass neutron star. A sufficiently faint stellar companion can only be made feasible by significantly reducing the distance to $\simeq 3.5$ kpc while simultaneously increasing the mass ratio to $q \simeq 0.3$, despite the multiple lines of evidence for $q \simeq 0.2$.

Key words: stars: black holes – (stars:) binaries: spectroscopic – stars: individual: 2MASS J04123153+6738486

1 INTRODUCTION

The mass distribution of neutron stars and stellar mass black holes is closely tied to the evolution of massive stars and supernovae (e.g., Sukhbold et al. 2016; Pejcha & Thompson 2015; Woosley et al. 2020). The relationship between the pre-supernova mass of the massive star and the type of the compact remnant left behind is complicated and depends on the chemical composition of the star, mass-loss rates, supernova explosion physics and binary interactions (e.g., Sukhbold et al. 2016; Patton et al. 2021). For example, massive stars that explode as Type IIp supernovae and form neutron stars have masses in the range $\sim 8.4 - 18.6\ M_\odot$ (e.g., Kochanek 2020). However, the population of massive stars that produce BHs is largely unconstrained except for the $\sim 20 - 25\ M_\odot$ progenitor of the failed supernovae candidate NGC6946-BH1 (e.g., Adams et al. 2017; Basinger et al. 2021). This complicates our understanding of the predicted BH mass function at birth (Woosley et al. 2020). While the fates of these massive stars are hard to predict, dead massive stars have left behind a plethora of compact remnants in our Galaxy – there are about $\sim 10^8$ stellar mass BHs and $\sim 10^9$ neutron stars in the Milky Way (Brown & Bethe 1994).

A well characterized sample of neutron stars and black holes is necessary to better understand massive stars. However, this is a challenging task because the vast majority of compact objects are electromagnetically dark. To date, most mass measurements for neutron stars and black holes come from pulsar and accreting binary systems selected from radio, X-ray, and gamma-ray surveys (see, for e.g., Champion et al. 2008; Liu et al. 2006; Özel et al. 2010; Farr

★ E-mail: jayasinghearachchilage.1@osu.edu

et al. 2011), and from the LIGO/Virgo detections of merging systems (see, for e.g., The LIGO Scientific Collaboration et al. 2021; Abbott et al. 2016, 2017). The populations of BHs observed as X-ray binaries and mergers are both heavily biased samples. For X-ray binaries, the companion must either fill its Roche lobe or have a modest separation and a strong wind. Compact objects discovered through gravitational wave observations come from the very small fraction of surviving binaries that are on very short orbits leading to a merger. These interacting systems are, however, a small minority of compact object binaries, and the far larger population of non-interacting systems is essentially unexplored. While non-interacting binaries are harder to find, they must be discovered and characterized in order to fully understand the numbers, properties, formation mechanism and evolutionary paths of the interacting systems.

Only a handful of convincing non-interacting compact objects have been discovered thus far. Three non-interacting BH candidates have been discovered in globular clusters: one by Giesers et al. (2018) in NGC 3201 (minimum black hole mass $M_{\rm BH} = 4.36 \pm 0.41\,{\rm M}_{\odot}$), and two by Giesers et al. (2019) in NGC 3201 ($M_{\rm BH}\sin(i) = 7.68 \pm 0.50\,{\rm M}_{\odot}$ and $M_{\rm BH}\sin(i) = 4.4 \pm 2.8\,{\rm M}_{\odot}$). These globular cluster systems likely have formation mechanisms that are very different from those of field black hole binaries because the high stellar densities allow formation mechanisms which do not operate for field stars.

Two non-interacting BH candidates have been found in the field. Thompson et al. (2019) discovered a low-mass ($M_{\rm BH} \simeq 3.3^{+2.8}_{-0.7}\,M_{\odot}$) non-interacting black hole candidate in the field on a circular orbit at ${\rm P_{orb}} \sim 83$ d around a spotted giant star. More recently, Jayasinghe et al. (2021b) discovered a non-interacting black hole candidate in the nearby binary V723 Mon ($d \simeq 460$ pc). This low mass gap BH candidate ($M_{\rm BH} = 3.04 \pm 0.06\,M_{\odot}$) is on a nearly edge-on ${\rm P_{orb}} = 59.9$ d circular orbit around a red giant. V723 Mon is an ellipsoidal variable and the binary parameters derived from the photometric variability were later confirmed in the models of the radial velocity residuals created by the ellipsoidal variability (Masuda & Hirano 2021).

A few other claims for non-interacting BH systems have been ruled out. The binary LB-1 was initially thought to host an massive stellar black hole ($M_{\rm BH} \simeq 68^{+11}_{-3}\,M_{\odot}$, Liu et al. 2019), but was later found to have a much less massive companion that was not necessarily a compact object (see, for e.g., Shenar et al. 2020; Irrgang et al. 2020; Abdul-Masih et al. 2020; El-Badry & Quataert 2020b). The naked-eye system HR 6819 was claimed to be a triple system with a detached black hole with $M_{\rm BH} = 6.3 \pm 0.7\,M_{\odot}$ (Rivinius et al. 2020), but was later found to be a binary system with a rapidly rotating Be star and a slowly rotating B star (El-Badry & Quataert 2020a; Bodensteiner et al. 2020). Recently, NGC 1850 BH1 was claimed to be a binary displaying ellipsoidal variability in the LMC with $M_{\rm BH} = 11.1^{+2.1}_{-2.4}\,M_{\odot}$ (Saracino et al. 2021), but was later argued to be a stripped B star binary (El-Badry & Burdge 2021). The common theme to these cases is an overestimate of the mass of the observed star based on its luminosity and the assumption of single star evolution for a binary where mass transfer has greatly reduced the mass of the more luminous star. Another example of a BH imposter was the system NGC 2004 #115, claimed to be a triple system consisting of a Be star on a tertiary orbit and an inner binary of a B star and a $\simeq$25 $M_{\odot}$ black hole (Lennon et al. 2021). El-Badry et al. (2021) later argued that the orbital inclination was underestimated by assuming tidal synchronization, and that the companion to the B star was more likely a $\sim 2-3\,M_{\odot}$ main sequence star.

Rapid advances in time-domain astronomy and precision *Gaia* astrometry (Lindegren et al. 2021a) provide promising pathways for future discoveries of non-interacting compact objects. For example, Chawla et al. (2021) estimated that $\sim 30-300$ non-interacting black holes are detectable in binaries around luminous companions using astrometry from *Gaia*. Similarly, Shao & Li (2019) used binary population synthesis models to estimate that there are $\sim 10^3$ detached non-interacting black holes in the Milky Way, with 10^2 of these systems having luminous companions that are brighter than $G \sim 20$ mag. In addition to astrometry, targeted searches combining high-cadence photometry and sparsely sampled radial velocities from wide-field time-domain surveys are a promising method to discover more systems (e.g., Thompson et al. 2019; Zheng et al. 2019; Rowan et al. 2021; Trimble & Thorne 1969). Based on the discovery of V723 Mon, we estimated that the Milky Way should contain 100-1000 similar systems (Jayasinghe et al. 2021b).

2M04123153+6738486 (hereafter 2M0412) is a luminous red-giant in the Camelopardalis constellation with J2000 coordinates $(\alpha, \delta) = (63.13141144391°, 67.64683129470°)$. It was first classified as an 'NSINE' variable star (ATO J063.1314+67.6468) in the the Asteroid Terrestrial-impact Last Alert System (ATLAS; Tonry et al. 2018; Heinze et al. 2018) catalog of variable stars with a period of ~80.36 days. It was classified as a semi-regular variable (ASASSN-V J041231.49+673848.6, ZTF J041231.52+673848.6) by the All-Sky Automated Survey for SuperNovae (ASAS-SN; Jayasinghe et al. 2018, 2021a; Shappee et al. 2014), and the Zwicky Transient Facility (ZTF; Chen et al. 2020; Bellm et al. 2019) with periods of ~40.65 days and ~41.20 days respectively.

2M0412 has 4 radial velocity measurements in the Apache Point Observatory Galactic Evolution Experiment DR16 (APOGEE; Gunn et al. 2006; Blanton et al. 2017; Wilson et al. 2019) with a maximum velocity difference of ${\rm \Delta RV_{max}} \sim 76$ km/s and a maximum observed acceleration between epochs of ~1.7 km/s/day (Thompson et al. 2019). This led us to re-examine the light curves to realize that 2M0412 was in fact an ellipsoidal variable with an ~81 day period. The radial velocity data and the orbital period from the light curves implied a mass function of $f(M) \simeq 0.5\,M_{\odot}$, which led us to investigate the system in detail.

Here we discuss our likely discovery of a massive $\sim 2-3\,M_{\odot}$ companion to the red giant in 2M0412. We describe the archival data and new observations used in our analysis in Section 2. In Section 3, we analyze the photometric and spectroscopic observations to derive the parameters of the binary system and the red giant secondary. In Section 4, we discuss the nature of the companion. We present a summary of our results in Section 5.

2 OBSERVATIONS

Here we present observations, both archival and newly acquired, that are used in our analysis of 2M0412.

2.1 Distance, Kinematics and Extinction

In *Gaia* EDR3 (Gaia Collaboration et al. 2020), 2M0412 is `source_id`=4904508754036203 52. Its raw EDR3 parallax of $\varpi_{\rm EDR3} = 0.2310 \pm 0.0130$ mas implies a distance of $d = 1/\varpi = 4329 \pm 245$ pc. We correct the reported EDR3 parallax using the zero-point correction ($\simeq 39.89\,\mu$as) described in Lindegren et al. (2021a) which is dependent on the color, magnitude, and sky position[1].

[1] We calculate the parallax zero-point using the python script provided in https://gitlab.com/icc-ub/public/gaiadr3_zeropoint

With this correction, we obtain $\varpi_{\rm EDR3,L21} = 0.2709 \pm 0.0130$ mas ($d = 1/\varpi = 3691 \pm 178$ pc). The global zero-point parallax offset in EDR3 is -17 μas (Lindegren et al. 2021b), and if we instead use this correction, we obtain $d = 1/\varpi = 4032 \pm 212$ pc. The zero-point correction from Lindegren et al. (2021a) differs from the global zero-point correction by ~ -23 μas. However, the zero-point correction from Lindegren et al. (2021a) can over-correct the parallax by $\sim 15 - 25$ μas (e.g., Groenewegen 2021; Bhardwaj et al. 2021; Zinn 2021). The probabilistic photogeometric distance estimate from Bailer-Jones et al. (2021) is $d = 3743^{+133}_{-161}$ pc. The spectrophotometric parallax estimate from Hogg et al. (2019) is $\varpi_{\rm spec} = 0.2284 \pm 0.0106$ mas ($d = 1/\varpi = 4378 \pm 204$ pc). The astrometric solution does not show significant excess noise and its renormalized unit weight error (RUWE) of 1.046 is not indicative of problems in the parallax or strong resolved binary motion. We adopt a distance of $d = 4$ kpc as our default, but the distance is the most important uncertainty for our conclusions and we discuss its impact on the inferred masses in § 3.3 (Table 6).

At this distance, 2M0412 is ~830 pc above the midplane. Its proper motion in EDR3 is $\mu_\alpha = -0.346 \pm 0.008$ mas yr^{-1}, and $\mu_\delta = 0.686 \pm 0.011$ mas yr^{-1}. Combining this with the systemic radial velocity from §3.2, the definition of the local standard of rest (LSR) from Schönrich et al. (2010), and using `BANYAN` (Gagné et al. 2018) for the calculations, the 3D space motion of 2M0412 relative to the LSR is $(U, V, W)_{\rm LSR} = (45.2, -19.5, -5.1)$ km s^{-1}. We calculated the thin disk, thick disk and halo membership probabilities based on these velocities following Ramírez et al. (2013) to obtain $P(\text{thin}) \simeq 98.5\%$, $P(\text{thick}) \simeq 1.5\%$ and $P(\text{halo}) \simeq 0\%$, respectively. This suggests that this system is a kinematically normal object in the thin disk.

2.2 Light Curves

We analyzed well-sampled light curves from ASAS-SN, ATLAS and ZTF, along with a densely sampled but phase-incomplete light curve from the Transiting Exoplanet Survey Telescope (TESS).

The ASAS-SN (Shappee et al. 2014; Kochanek et al. 2017) survey obtained V-band and g-band light curves of 2M0412 spanning from December 2014 to November 2021 (~31 orbits). 2M0412 clearly varies in the ASAS-SN light curves, with two equal maxima and two minima when phased with the orbital period. We determined the photometric period using `Period04` (Lenz & Breger 2005). The dominant ASAS-SN periods of $P_{\rm ASAS-SN,V} = 40.5930 \pm 0.0572$ d and $P_{\rm ASAS-SN,g} = 40.6090 \pm 0.08442$ d correspond to $P_{\rm orb}/2$ for ellipsoidal variability. We find an orbital period of

$$P_{\rm orb,ASAS-SN\ V} = 81.1861 \pm 0.2287\,{\rm d}. \quad (1)$$

We retrieved g and $r-$band photometry from the ZTF DR7 catalog (Masci et al. 2019) spanning April 2018 to April 2021 (~13 orbits). The dominant periods in the ZTF data, $P_{\rm ZTF,g} = 40.7195 \pm 0.0770$ d, $P_{\rm ZTF,r} = 40.5224 \pm 0.0753$ d, again correspond to $P_{\rm orb}/2$. We also retrieved photometry from the ATLAS survey (Tonry et al. 2018) in the ATLAS 'c' (cyan) and 'o' (orange) filters. The ATLAS observations span from August 2017 to March 2021 (~16 orbits). We obtain photometric periods of $P_{\rm ATLAS,c} = 40.5497 \pm 0.0633$ d, $P_{\rm ATLAS,o} = 40.5447 \pm 0.0627$ d. The differences between the ASAS-SN, ZTF and ATLAS photometric period estimates are not statistically significant.

2M0412 (`TIC 102780470`) was observed by *TESS* (Ricker et al. 2015) in Sector 19, and the 27 days of observations span [0.22,0.52] in orbital phase where the phase of the RV maximum is 0.75. We analyzed the *TESS* data using the adaptation of the ASAS-SN image subtraction pipeline for analyzing *TESS* full-frame images (FFIs) described in Vallely et al. (2020). The light curve does not include epochs where the observations were compromised by the spacecraft's momentum dump maneuvers.

Figures 1 and 2 present the ASAS-SN, ATLAS, ZTF and *TESS* light curves for 2M0412 phased at the orbital period of $P_{\rm orb} \simeq 81.2$ d. When phased with the orbital period, the light curves have two equal maxima and two unequal minima, which is typical of ellipsoidal variability. The light curves in the bluer filters tend to have more scatter than those in the redder filters.

2.3 UV photometry

We obtained Swift UVOT (Roming et al. 2005) images in the $UVM2$ (2246 Å) band (Poole et al. 2008) through the Target of Opportunity (ToO) program (Target ID number 14417). We only obtained images in the $UVM2$ band because the *Swift* $UVW1$ and $UVW2$ filters have significant red leaks that make them unusable in the presence of the emission from the cool giant. Each epoch of UVOT data includes multiple observations, which we combined using the `uvotimsum` package. We then used `uvotsource` to extract source counts using a 5.″0 radius aperture centered on the star. We measured the background counts using a source-free region with a radius of 40.″0 and used the most recent calibrations (Poole et al. 2008; Breeveld et al. 2010) and taking into account the recent update to the sensitivity corrections for the *Swift* UV filters[2]. We were unable to detect 2M0412 in the *Swift* $UVM2$ data. The $UVM2$ observations are summarized in Table 1.

2M0412 was previously observed as part of the *GALEX* Medium Imaging survey (MIS) and All-Sky Imaging Survey (AIS) in January 2011 and January 2004, respectively (Morrissey et al. 2007). As part of the MIS survey, 2M0412 was observed for 1689 seconds in the NUV filter. Additionally, 2M0412 was observed for 232 seconds in both the *NUV* and *FUV* filters. We do not detect 2M0412 in any of the *GALEX* images. In the *NUV*, we adopt the 22.7 AB mag 5σ upper limit from the longer MIS exposure (Bianchi et al. 2014). In the *FUV*, we adopt the 19.9 AB mag 5σ upper limit from the AIS exposure. The *GALEX* observations are summarized in Table 1.

2.4 Spectroscopic observations

To better sample the radial velocities, we obtained 10 additional spectra. These observations, along with the archival APOGEE DR16 observations, are summarized in Table 2. Using the HIRES instrument (Vogt et al. 1994) on Keck I, we obtained 8 spectra with $R \approx 60000$ between Aug 14 2021 and Nov 19 2021 using the standard California Planet Search (CPS) setup (Howard et al. 2010). The exposure times ranged from 292 to 515 seconds. We also obtained very high resolution ($R \approx 130,000$) spectra on 10 Sep 2021 and 02 Oct 2021 using the Potsdam Echelle Polarimetric and Spectroscopic Instrument (PEPSI; Strassmeier et al. 2015) on the Large Binocular Telescope. We used the 200 μm fiber and 2 cross-dispersers (CD). The data were processed as described in Strassmeier et al. (2018). The total integration time for each epoch was 70 minutes, and the 2 CDs cover the wavelength ranges 4758 – 5416 Å and 6244 – 7427 Å. The HIRES, PEPSI and MODS observations are summarized in Table 2.

[2] `https://www.swift.ac.uk/analysis/uvot/index.php`

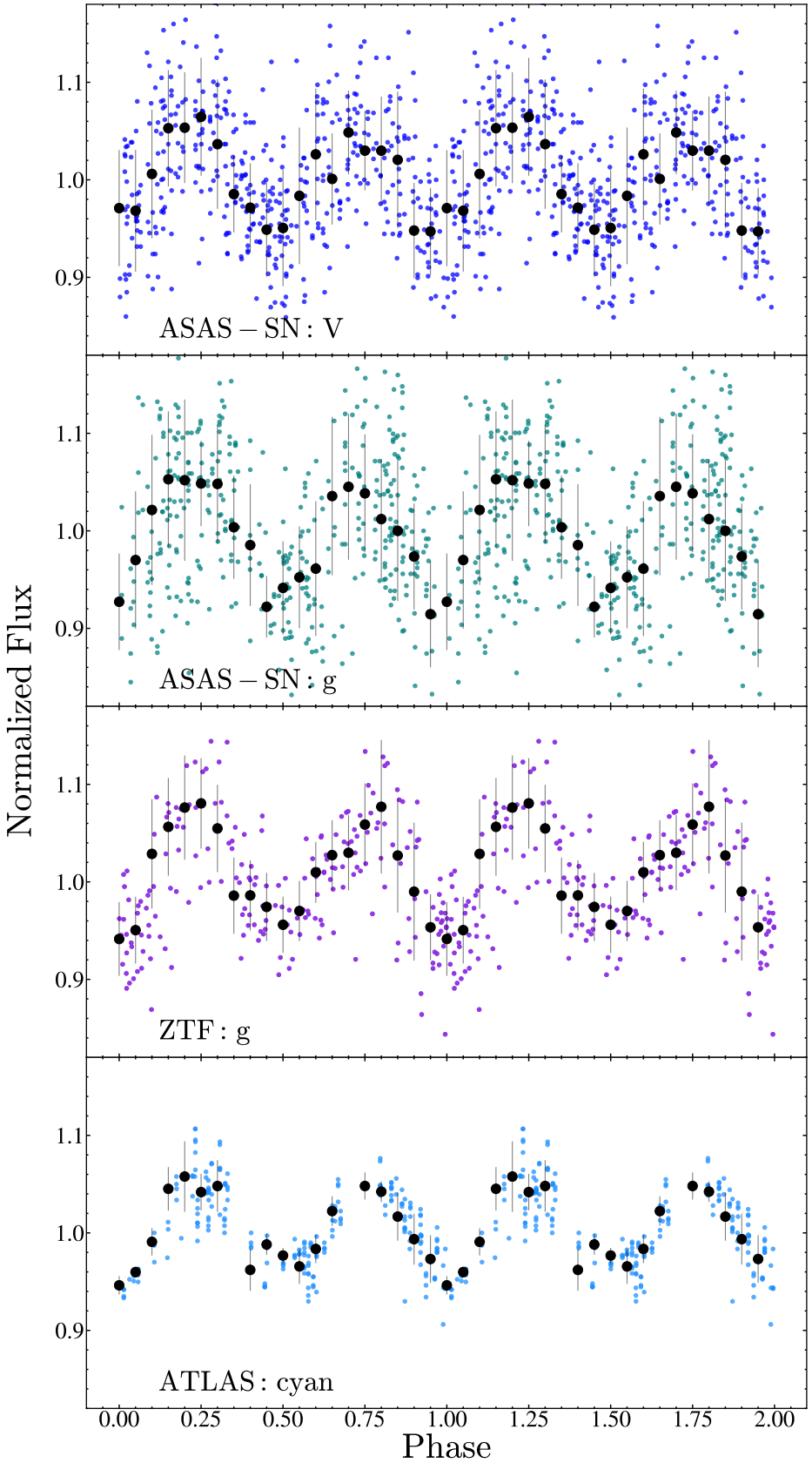

Figure 1. The normalized ASAS-SN V, ASAS-SN g, ZTF g and ATLAS c-band light curves for 2M0412 as a function of orbital phase (defined with the epoch of maximum RV at $\phi = 0.75$). The binned light curve for each data set is shown in black. The error bars for the binned light curve show the standard deviation in each bin.

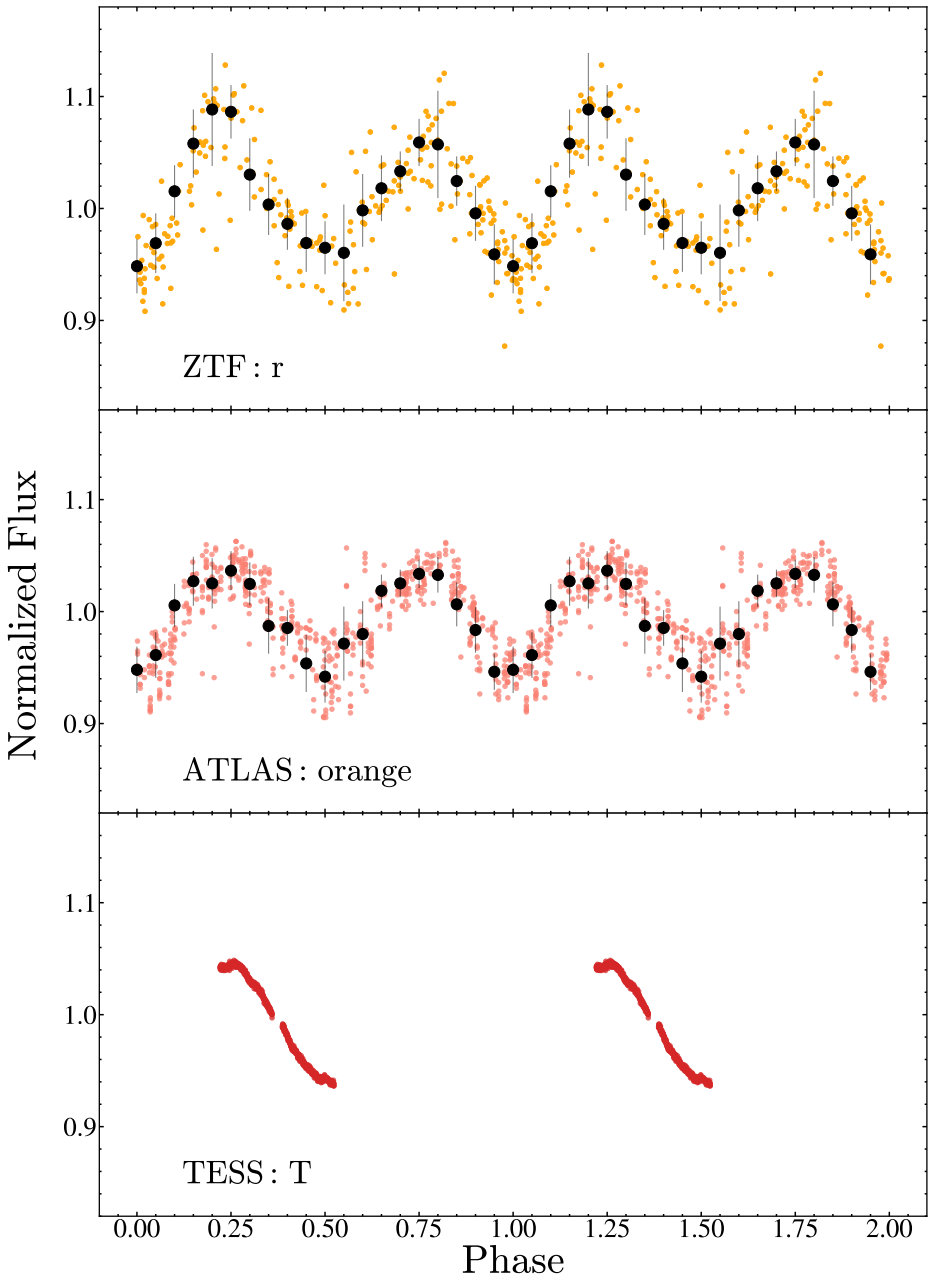

Figure 2. The normalized ZTF r, ATLAS o and *TESS* T-band light curves for 2M0412. The format is the same as Figure 1.

Table 1. *GALEX* and *Swift* UV observations

JD	Date	Phase	Filter	AB mag limit	σ
2459453.807	2021-08-27	0.076	*Swift UVM2*	> 22.78	3σ
2459488.654	2021-10-01	0.506	*Swift UVM2*	> 22.67	3σ
2455572.568	2011-01-11	0.259	*GALEX NUV* (MIS)	> 22.7	5σ
2453017.625	2004-01-13	0.782	*GALEX FUV* (AIS)	> 19.9	5σ

2.5 X-ray data

We analyzed the X-ray observations from the *Swift* X-Ray Telescope (XRT; Burrows et al. 2005) taken simultaneously with the *UVM2* observations. Individual exposure times ranged from 120 to 1650 seconds, for a total of 4010 seconds. All XRT observations were reprocessed using the *Swift* XRTPIPELINE version 0.13.2 and standard

Table 2. Radial velocities from APOGEE DR16, HIRES, and PEPSI.

BJD (TDB)	Date	Phase	RV (kms^{-1})	σ_{RV} (kms^{-1})	Instrument
2457279.99438	2015-09-14	0.295	−86.888	0.031	APOGEE DR16
2457292.96813	2015-09-27	0.455	−59.246	0.016	APOGEE DR16
2457320.92338	2015-10-25	0.799	−7.964	0.023	APOGEE DR16
2457323.87005	2015-10-28	0.835	−11.194	0.017	APOGEE DR16
2459441.12722	2021-08-14	0.920	−26.94	0.10	HIRES
2459442.11471	2021-08-15	0.932	−30.43	0.10	HIRES
2459457.11748	2021-08-30	0.117	−74.32	0.10	HIRES
2459467.98696	2021-09-10	0.251	−87.423	0.060	PEPSI
2459472.12548	2021-09-14	0.302	−86.11	0.10	HIRES
2459485.12694	2021-09-27	0.462	−57.29	0.10	HIRES
2459489.96760	2021-10-02	0.522	−41.928	0.034	PEPSI
2459502.97527	2021-10-15	0.682	−9.84	0.10	HIRES
2459511.98487	2021-10-24	0.793	−7.61	0.10	HIRES
2459537.92734	2021-11-19	0.113	−73.81	0.10	HIRES

filter and screening criteria[3] and the most up-to-date calibration files. To increase the signal to noise of our observations, we combined all cleaned individual XRT observations using XSELECT version 2.4g. To place constraints on the presence of X-ray emission (see §3.6), we used a source region with a radius of 30 arcsec centered on the position of 2M0412 and a source-free background region with a radius of 150 arcsec located at RA = 04:12:38.10, Dec = 67:43:00.86 (J2000).

3 RESULTS

Here we present our analyses of the observations described in §2. In §3.1, we characterize the red giant using its spectral energy distribution (SED) and spectra. In §3.2, we fit Keplerian models to the radial velocities and derive a spectroscopic orbit for 2M0412. In §3.3, we model the ellipsoidal variations of the red giant using multi-band light curves and the binary modeling tools ELC and `PHOEBE` to derive the masses of the red giant and the companion. In §3.4, we discuss a secondary component in the radial velocity cross-correlation function. In §3.5, we discuss the broad Balmer Hα emission and its orbital phase dependent variability. In §3.6, we discuss the X-ray observations.

3.1 Properties of the Red Giant

We characterized the red giant using both fits to its overall SED and analyses of the available spectra. For the SED, we used photometry from APASS DR10 (Henden et al. 2018), Pan-STARRS DR1 Chambers et al. (2016), 2MASS (Skrutskie et al. 2006) and All-WISE (Wright et al. 2010). We used the *Swift UVM2* and *GALEX* NUV photometry as upper limits. The compilation of the multi-band photometry used in these fits are given in Table 3.

We fit the SED of 2M0412 using DUSTY (Ivezic & Elitzur 1997; Elitzur & Ivezić 2001) inside a MCMC wrapper (Adams & Kochanek 2015). We assumed only foreground extinction due to $R_V = 3.1$ dust (Cardelli et al. 1989) and used the ATLAS9 (Castelli & Kurucz 2003) model atmospheres for the star. We assume that the source is at a distance of 4.0 kpc and used minimum luminosity uncertainties of 10% for each band to compensate for any systematic errors and for the observed variability. We used a temperature prior based on APOGEE DR16 of $T_{\rm eff,giant} = 4188 \pm 75$ K and a prior of $E(B-V) = 0.54 \pm 0.10$ on the extinction from `mwdust` (Bovy et al. 2016; Marshall et al. 2006; Drimmel et al. 2003; Green et al. 2019). Ignoring the upper limits, we are fitting 11 photometric bands with three variables (L_*, T_* and $E(B-V)$) and two priors, leading to a best fit with $\chi^2 = 3.8$ for 10 degrees of freedom. The SED fit yields $T_{\rm eff,giant} \simeq 4207 \pm 68$ K, $L_{\rm giant} = 229 \pm 15\ L_\odot$, $R_{\rm giant} \simeq 28.5 \pm 0.6\ R_\odot$ and $E(B-V) = 0.587 \pm 0.046$ mag. Figure 3 shows the SED and the best fitting model. The SED well-constrains the temperature and is consistent with the extinction estimates.

If we require any companion to be fainter than the 3σ UVM2 limit and contribute less than 20%, 10%, 30%, 30% of the light in the g, i, J and K_s bands, we can constrain the mass of any companion as in Jayasinghe et al. (2021b). We took [Fe/H] = −0.5 PARSEC (Bressan et al. 2012) isochrones and found the maximum mass star at each age which would satisfy these constraints as a limit on single stars. We also considered twin binaries, consisting of two equal mass stars, to obtain an upper mass limit for stellar binary companions (Trimble & Thorne 1969). For a single main sequence star, the maximum allowed mass is $M_* \lesssim 1.4\ M_\odot$. If we allow the star to be a subgiant, this increases to $M_* \lesssim 1.7\ M_\odot$. For models with two stars, the limit is a twin main sequence binary with a total mass $M_{\rm binary} \lesssim 2.6\ M_\odot$ ($M_{\rm binary} \lesssim 2.8\ M_\odot$ for a twin subgiant binary).

The APOGEE, HIRES and PEPSI spectra indicate that the giant is rapidly rotating. The APOGEE DR16 spectra were used to measure $v_{\rm rot} \sin i = 12.61 \pm 0.92\,{\rm km\,s^{-1}}$ following the methods described in Tayar et al. (2015); Dixon et al. (2020); Mazzola Daher et al. (2021). The HIRES CPS pipeline (Petigura 2015) reports $v_{\rm rot} \sin i = 13.3 \pm 1.0\,{\rm km\,s^{-1}}$ and we found $v_{\rm rot} \sin i = 12.8 \pm 1.2\,{\rm km\,s^{-1}}$ from the PEPSI spectrum using `iSpec` (Blanco-Cuaresma et al. 2014; Blanco-Cuaresma 2019). Assuming that the rotation of the giant is tidally synchronized with the orbit, we can derive the rotational velocity of the giant using a radius of $R_{\rm giant} = 30\ R_\odot$ as

$$v_{\rm rot} = \frac{2\pi R_{\rm giant}}{P_{\rm rot}} = 18.7 \pm 0.4\,{\rm km\,s^{-1}} \left(\frac{\rm R_{giant}}{30\ \rm R_\odot}\right). \quad (2)$$

This is a reasonable assumption because binaries with evolved components ($\log(g) < 2.5$) and orbital periods shorter than ~100 days are expected to be tidally locked (e.g., Verbunt & Phinney 1995; Price-Whelan & Goodman 2018). However, the light curve residuals after removing the ellipsoidal variability show no periodic signal

[3] http://swift.gsfc.nasa.gov/analysis/xrt_swguide_v1_2.pdf

Table 3. Multi-band photometry measurements used in the construction of the SED for 2M0412. Luminosities for each band are calculated assuming a nominal distance of $d \simeq 4.0$ kpc. The fluxes and luminosities have not been corrected for extinction.

Filter	Magnitude	σ	F_λ [ergs s^{-1} cm^{-2} Å^{-1}]	λL_λ [$L_\odot$]	Reference
GALEX FUV	> 19.9	5σ	$< 7.1 \times 10^{-13}$	< 0.346	AIS; Bianchi et al. (2014)
GALEX NUV	> 22.7	5σ	$< 2.5 \times 10^{-13}$	< 0.017	MIS; Bianchi et al. (2014)
Swift UVM2	> 22.8	3σ	$< 1.0 \times 10^{-14}$	< 0.005	This work
Johnson B	16.34	0.05	1.1×10^{-12}	4.7	Henden et al. (2018)
Johnson V	14.39	0.04	1.5×10^{-12}	19.6	Henden et al. (2018)
Pan-STARRS g	15.15	0.01	3.5×10^{-15}	11.3	Chambers et al. (2016)
Pan-STARRS r	13.55	0.01	9.5×10^{-15}	39.0	Chambers et al. (2016)
Pan-STARRS i	13.02	0.01	1.0×10^{-14}	51.8	Chambers et al. (2016)
Pan-STARRS z	12.50	0.01	1.3×10^{-14}	69.8	Chambers et al. (2016)
Pan-STARRS y	12.14	0.01	1.4×10^{-14}	88.5	Chambers et al. (2016)
2MASS J	10.81	0.02	1.3×10^{-14}	105.5	Skrutskie et al. (2006)
2MASS H	9.94	0.02	1.0×10^{-14}	114.7	Skrutskie et al. (2006)
2MASS K_s	9.69	0.02	4.9×10^{-15}	70.8	Skrutskie et al. (2006)
WISE W1	9.47	0.02	1.1×10^{-15}	25.1	Wright et al. (2010)
WISE W2	9.52	0.02	3.2×10^{-16}	10.1	Wright et al. (2010)
WISE W3	9.37	0.04	1.0×10^{-17}	0.8	Wright et al. (2010)
WISE W4	> 8.29	2σ	$< 2.2 \times 10^{-18}$	< 0.3	Wright et al. (2010)

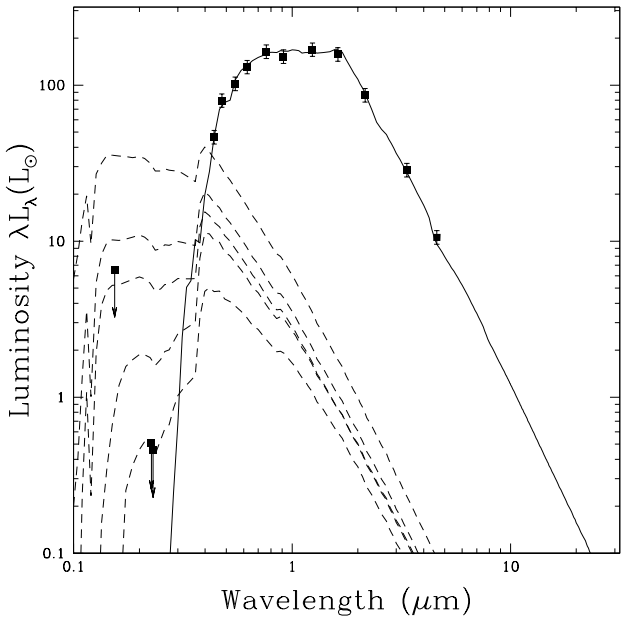

Figure 3. The best-fitting, extinction-corrected SED model for 2M0412. The 1σ *Swift UVM2* and *GALEX FUV/NUV* upper limits are shown as arrows. The SEDs for main sequence stars of masses 1.3 $M_\odot$ (1 Gyr), 1.5 $M_\odot$ (1 Gyr), 1.8 $M_\odot$ (0.1 Gyr), 2.0 $M_\odot$ (0.1 Gyr) and 2.5 $M_\odot$ (0.1 Gyr) are also shown. As shown by these SEDs, single main sequence companion stars with masses $\gtrsim 1.4$ $M_\odot$ are easily ruled out.

that might confirm or reject this hypothesis. The APOGEE DR16, HIRES and PEPSI measurements combined with the period and stellar radius yield estimates of $\sin i = 0.67 \pm 0.05$, $\sin i = 0.71 \pm 0.05$ and $\sin i = 0.68 \pm 0.06$, respectively, and orbital inclinations of $i = 42.1 \pm 3.9°$, $i = 45.2 \pm 4.1°$ and $i = 42.8 \pm 4.7°$, respectively.

To derive the surface temperature ($T_{\rm eff}$), surface gravity ($\log(g)$), and metallicity ([Fe/H]) of the giant, we use the spectral synthesis code `iSpec`. `iSpec` fits the observed spectra with synthetic spectra generated by `SPECTRUM` (Gray & Corbally 1994) using MARCS model atmospheres (Gustafsson et al. 2008). The line lists used in this process span the wavelength range from 480 nm to 680 nm. We fit all the HIRES spectra keeping the microturbulent velocity $v_{\rm mic}$ as a free parameter and report the median and standard deviation in each parameter. The wavelength range of the PEPSI spectra do not cover many of the lines that are optimal for spectroscopic parameter determination, so we do not fit these data. `iSpec` estimates the macroturbulent velocity analytically based on $T_{\rm eff}$ and $\log(g)$. We obtain $T_{\rm eff,giant} = 4367 \pm 48$ K, $\log(g) = 1.24 \pm 0.27$, [Fe/H] $= -0.51 \pm 0.08$, and [α/Fe] $= 0.23 \pm 0.10$, and $v_{\rm micro} = 1.11 \pm 0.19$ km s^{-1}. The spectroscopic parameters derived for the giant are summarized in Table 4. These estimates of the spectroscopic parameters do not consider the effects of veiling on the observed spectrum. Veiling introduces systematic uncertainties on these parameters and will lower the temperature estimate.

Binaries with a compact object companion frequently have an additional source of diluting ("second") light, typically due to an accretion disk (e.g., Hynes et al. 2005; Wu et al. 2015; Jayasinghe et al. 2021b). To estimate the veiling present in the spectra, we selected the HIRES spectrum with the deepest absorption lines (at phase 0.1), subtracted the best-fit synthetic spectrum from 500 nm to 620 nm and calculated the residuals in normalized flux. Next, we binned the residuals in bins of 2 nm and calculated the 5$^{\rm th}$ percentile in residual flux. We fit the binned residual fluxes using a polynomial of the form $F = m\,\lambda + C$. Using this fit, we estimate that the veiling flux at 500 nm and 620 nm contributes ~17%, and ~8%, to the total flux. We estimate the veiling fluxes in the g, V and r bands as ~19%, ~13%, and ~7%, respectively. This fit yields an unphysical, negative veiling flux when extrapolated to the *TESS* band, so for simplicity, we assume that the veiling at redder wavelengths is negligible.

The APOGEE ASPCAP pipeline routinely overestimates $\log(g)$ for rapidly rotating giants because the ASPCAP template library of synthetic spectra does not include rotation for giants. For giants rotating at $v_{\rm rot} \sin i \sim 8 - 14$ km s^{-1}, the offset in $\log(g)$ can be as large as 0.1-0.5 dex (see, e.g., Thompson et al. 2019). This bias can also affect other spectroscopically determined parameters for these rapidly rotating stars. Therefore, we adopt the parameters from fitting the optical HIRES spectra with `iSpec` as our standard.

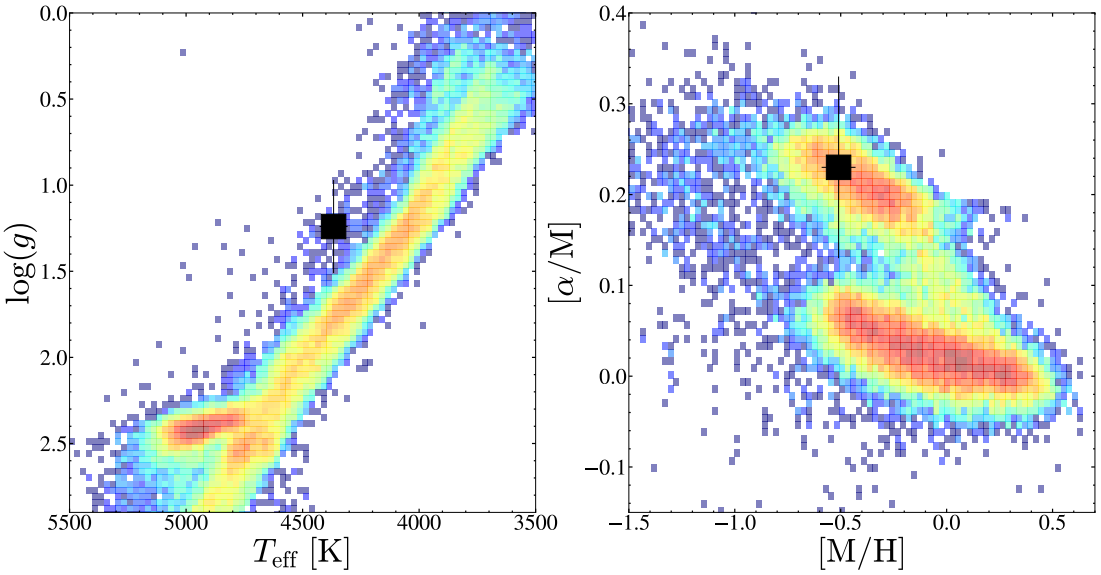

Figure 4. *Left:* $\log(g)$ vs. $T_{\rm eff}$ for the sample of APOGEE DR16 giants with $-0.75 < [{\rm M/H}] < -0.25$, *Right:* $[\alpha/{\rm M}]$ vs. $[{\rm M/H}]$ for the sample of APOGEE DR16 giants with $1.2 < \log(g) < 3$ and $3900 < T_{\rm eff} < 4500$ K. The position of the giant is shown in black. Based on its location in these figures, 2M0412 is a typical high-α red giant.

We use the spectroscopic parameters derived from the optical HIRES spectra (Table 4), the *Gaia* parallax, and the $BVJHK_s$ photometry used in the SED fit as priors to infer the physical properties of the giant using the MESA Isochrones and Stellar Tracks (MIST; Dotter 2016; Choi et al. 2016) and `isoclassify` (Huber et al. 2017; Berger et al. 2020) to derive stellar parameters through isochrone fitting. As the best fit, we obtain $M_{\rm giant} = 1.11^{+0.24}_{-0.22}$ $M_\odot$, $R_{\rm giant} = 29.8^{+2.2}_{-2.0}$ $R_\odot$, $T_{\rm eff,giant} = 4306 \pm 39$ K, $d_{\rm giant} = 4301^{+318}_{-289}$ kpc, $L_{\rm giant} = 278^{+40}_{-37}$ $L_\odot$, $\log(g) = 1.5 \pm 0.1$, and an estimated age $\sim 4.6^{+5.3}_{-2.2}$ Gyr. These results are consistent with the properties of the giant derived from the spectra and the SED. However, in §3.3 we discuss evidence that the giant is stripped and that the mass as inferred from single star tracks is over-estimated.

The surface gravity of the giant determined from the spectroscopic analysis and isochrone fitting is consistent with that inferred from the `PHOEBE` models for the ellipsoidal variations presented in §3.3 ($\log(g)_{\rm PHOEBE} = 1.29 \pm 0.03$). Given the spectroscopic $\log(g)$ and the radius of the giant from those models (§3.3), the spectroscopic mass is $M_{\rm giant,spec} = 0.9 \pm 0.6$ $M_\odot$, consistent with the mass of the giant derived from the `PHOEBE` models. The spectroscopic temperature from the HIRES spectra is ∼100 K hotter than the estimates from `APOGEE` and the SED fits. Based on the van Belle et al. (1999) temperature scale for giants, our temperature estimates are consistent with a K3/K4 giant. The absolute V-band magnitude ($M_V \simeq -0.5 \pm 0.1$) is consistent with luminosity class III stars (Straizys & Kuriliene 1981). For single-star evolution, the spectroscopic measurement of $\log(g)$ suggests that the giant is currently evolving along the upper red giant branch (see Figure 4). The giant is more luminous than the red clump, implying that it has not yet undergone a helium flash. The position of the giant in the $[\alpha/{\rm M}]$–$[{\rm Fe/H}]$ space (Figure 4) indicates that the giant has abundances typical of the high-α abundance sequence.

Table 4. Properties of the red giant in 2M0412 as inferred from analyzing high-resolution spectra, SED fits, and comparison to MIST single star evolutionary tracks (Dotter 2016; Choi et al. 2016).

Parameter	APOGEE DR16/ASPCAP	HIRES/`iSpec`*
$T_{\rm eff}$ (K)	4187 ± 75	4367 ± 48
$\log(g)$	1.80 ± 0.06	1.24 ± 0.27
[Fe/H]	-0.73 ± 0.01	-0.51 ± 0.08
$[\alpha/{\rm Fe}]$	-0.04 ± 0.01	0.23 ± 0.10
$v_{\rm mic}$ (km s^{-1})	0.58 (fixed)	1.11 ± 0.19
$v_{\rm mac}$ (km s^{-1})	4.53 (fixed)	5.45 ± 0.31
$v_{\rm rot} \sin i$ (km s^{-1})*	not fitted	13.5 ± 1.0
R ($R_\odot$)	28.5 ± 0.6	
L ($L_\odot$)	230 ± 15	
M ($M_\odot$)	$1.11^{+0.24}_{-0.22}$	

* We report the median and standard deviation of the `iSpec` fits to the seven HIRES spectra.

3.2 Keplerian orbit models

We fit Keplerian orbits to the APOGEE DR16, HIRES and PEPSI radial velocities using two separate codes. First, we use `TheJoker` (Price-Whelan et al. 2017) Monte Carlo sampler. We first fit the joint data set using a broad uniform prior in period spanning [1 d,1000 d]. We obtain a unimodal solution at $P_{\rm orb} \simeq 82.6$ d, which is close to the orbital period from the light curves. We then reran `TheJoker` with a Gaussian prior on the period of $P_{\rm orb} = 81.2 \pm 0.5$ d. In these joint fits we also include additional parameters to allow for any velocity zero

point offsets between the three instruments and set the argument of periastron to $\omega = 0$ after confirming that there was no evidence for a non-zero ellipticity. The results of the fits are summarized in Table 5. The mass functions are well-constrained and mutually consistent, and the elliptical models yield a very small, non-zero ellipticity that is not significant. As a second, independent fit, we use the Yorbit genetic algorithm (Ségransan et al. 2011), frequently used in the discovery of extra-solar planets (e.g. Mortier et al. 2016; Martin et al. 2019). We find orbital parameters consistent with `TheJoker` results. In Fig. 5 we plot the Yorbit fit to the data.

For an edge on orbit and a typical giant mass of $M_{\rm giant} \simeq 1 M_\odot$, the companion mass is $M_{\rm comp} \simeq 1.6 M_\odot$. Using the inclination estimated from $v_{\rm rot} \sin i$ measurements from the high resolution spectra ($i \simeq 42°$), the companion mass is $M_{\rm comp} \simeq 3.3 M_\odot$ and the semi-major axis is $a_{\rm orb} \simeq 128 R_\odot$. The Roche limits are approximately $R_{\rm L,giant} = 0.28a \simeq 36 R_\odot$ for the giant and $R_{\rm L,comp} = 0.48a \simeq 63 R_\odot$ for the companion. Based on the radius estimate from the SED fits (§3.1), the giant is almost filling its Roche lobe ($R_{\rm giant}/R_{\rm L,giant} \simeq 0.9$) and it is in the regime where we should be seeing strong ellipsoidal variability due to the tidal deformation of the giant by the gravity of the companion (e.g., Morris 1985).

While we fit the RVs independently of the photometry here, for the remainder of this paper we use the orbit derived from the combined RV+light curve fits in §3.3. Given that the orbit is circular, we define the phase relative to the epoch of maximal radial velocity $T_{\rm RV,max} = 2457722.795 \pm 0.130$ d instead of the epoch of periastron. We define orbital phases so that $T_{\rm RV,max}$ corresponds to $\phi = 0.75$, the companion eclipses at $\phi = 0.5$ and the giant would be eclipsed at $\phi = 0$ for an edge-on orbit.

3.3 PHOEBE and ELC models of a giant + compact object binary

We interpret the light curves as ellipsoidal variability and fit models to derive the orbital properties and dynamical masses of the red giant and its companion. Here we focus on the scenario where 2M0412 is a giant with a faint companion. We run additional models for the giant with a visible companion in §3.4.

We initially tried MCMC fits of the ZTF r-band and TESS light curves using `ELC` (Orosz & Hauschildt 2000; Ter Braak 2006) and `PHOEBE` (Prša et al. 2016; Horvat et al. 2018; Conroy et al. 2020; Foreman-Mackey et al. 2013) with priors on the radius ($R_{\rm giant} = 29 \pm 1 R_\odot$), temperature ($T_{\rm eff,giant} = 4150 \pm 100$ K), surface gravity ($\log g = 1.2 \pm 0.3$) and rotation ($v_{\rm rot} \sin i = 13.5 \pm 1$ km/s) of the giant. In the `PHOEBE` models, we assume that the companion to the red giant is a compact object and fix it to be a small ($R = 3 \times 10^{-6}\ R_\odot$), cold ($T_{\rm eff} = 300$ K) black body, use the simplest and fastest eclipse model (`eclipse_method=only_horizon`). We do not consider the effects of irradiation and reflection in our models. We adopt a logarithmic limb-darkening law and use coefficients from Claret & Bloemen (2011) and Claret (2017).

We tried both fixing the period and simultaneously fitting the period and radial velocity data. Since the initial models suggested the giant was close to filling its Roche lobe, we also ran `PHOEBE` models with the giant constrained to be semi-detached. These models led to mass ratios of $q \simeq 0.20$ to 0.25 and inclinations of $i = 35°$ to 45°. All of the models settled on solutions where the radius of the giant was $\simeq 35\ R_\odot$, much larger than the SED-based prior ($29 \pm 1\,{\rm R}_\odot$). This appears to be driven by a combination of the other priors and the assumption of a semi-detached model (more below). Simultaneously fitting the RVs and light curves with `PHOEBE`, we constrained the orbit to $P_{\rm orb} = 81.16839^{+0.00044}_{-0.00045}$ d, $a_{\rm giant} \sin i = 67.103^{+0.029}_{-0.028}\ R_\odot$, and $v_\gamma = -47.316^{+0.011}_{-0.010}$ km s^{-1}.

In the fits to the ellipsoidal variability, a larger stellar radius drives higher masses. Even if the giant is not completely Roche-filling, it is close, and so a physically larger star forces a larger semi-major axis and thus a larger mass given the observed orbital period and radial velocity amplitude. With a giant radius as large as $R_{\rm giant} \simeq 35 R_\odot$, as returned from the semi-detached models, the giant is inferred to have a mass of order $M_{\rm giant} \sim 1\ M_\odot$ and the companion has a mass of order $M_{\rm comp} \sim 4\ M_\odot$. Because the giant's temperature is very well constrained, the only way to make the giant this large is to make it more luminous. For $R_{\rm giant} \simeq 35\,{\rm R}_\odot$, this requires a much larger distance of 4.7 kpc than the $\simeq 4.0$ kpc we adopted based on *Gaia*. In short, the fits to the ellipsoidal variability indicate that the giant's radius is the primary driver of our inference about the mass of the giant and its companion, which is in turn directly connected to the distance to the system.

Since the giant's radius is the controlling variable, we put our final focus on a series of `PHOEBE` models where the giant has fixed radii of $R_{\rm giant} = 23$, 25, 27, 29, 31, 33, and $35 R_\odot$, corresponding to distances of 3.2 to 4.7 kpc. We fix the orbit to the radial velocity solution from `PHOEBE` and the temperature of the giant to $T_{\rm eff,giant} = 4200$ K. We do not include priors on either $\log g$ or $v_{\rm rot} \sin i$. Table 6 presents the results. The reported errors are purely statistical and do not consider systematic effects (veiling, etc.) in the derivation of the binary solution.

While the inferred radius of the giant is always relatively close to the Roche limit, we see that $R_{\rm giant}/R_{\rm Roche}$ increases from 0.90 to 0.98 as $R_{\rm giant}$ increases from 23 to $35\ R_\odot$. This explains why the assumption of a semi-detached synchronized star drove the solution to larger giant radii (larger distance, larger luminosity) in our initial fits.

A synchronized, Roche lobe filling star satisfies the relation

$$v_{\rm rot} \sin i / K_{\rm giant} = 0.462\ q^{1/3} (1+q)^{2/3} \qquad (3)$$

(see, for e.g., Wade & Horne 1988; Torres et al. 2002). We found we could not analytically satisfy this constraint and $R_{\rm giant}/R_{\rm Roche} = 1$ for lower mass and physically smaller giants, confirming the modelling results that for smaller radii the giant cannot be Roche filling, cannot be in synchronous rotation, or both. Given that the orbit has circularized, it seems likely that the envelope of the giant is rotating synchronously.

Table 6 also reports the $v_{\rm rot} \sin i$ and $\log g$ estimates for each radius. The values of $\log g$ are almost independent of the giant's radius and consistent with the spectroscopic estimates. The values of $v_{\rm rot} \sin i$ increase as we increase the giant's radius. Like forcing a semi-detached geometry, larger $v_{\rm rot} \sin i$ pushes the models to larger giant radii and larger distances if tidal synchronization is imposed as a constraint, as we did in the initial semi-detached `PHOEBE` and `ELC` models.

A final important point is that for the models in Table 6, the mass ratio and inclination angle both decrease as the giant's radius decreases, such that even a model with $M_{\rm giant} \simeq 0.35\ M_\odot$ requires a $\simeq 2.1\ M_\odot$ companion. This is much larger than the limits from the SED for single-star companions, which require $M_{\rm comp} < 1.3\ M_\odot$ and $< 1.7\ M_\odot$ for main sequence and subgiant stars, respectively (§3.1, Fig. 3). While this value of the companion mass is below the upper limits on a *binary* star companion from the SED, binary models are ruled out by the observation of a second RV component in the system, which we describe in §3.4. We further note that even if the giant is heavily stripped, there is a hard lower limit to its mass of $\simeq 0.32\ M_\odot$ that is set by the minimum core mass given its luminosity, (eq. 9),

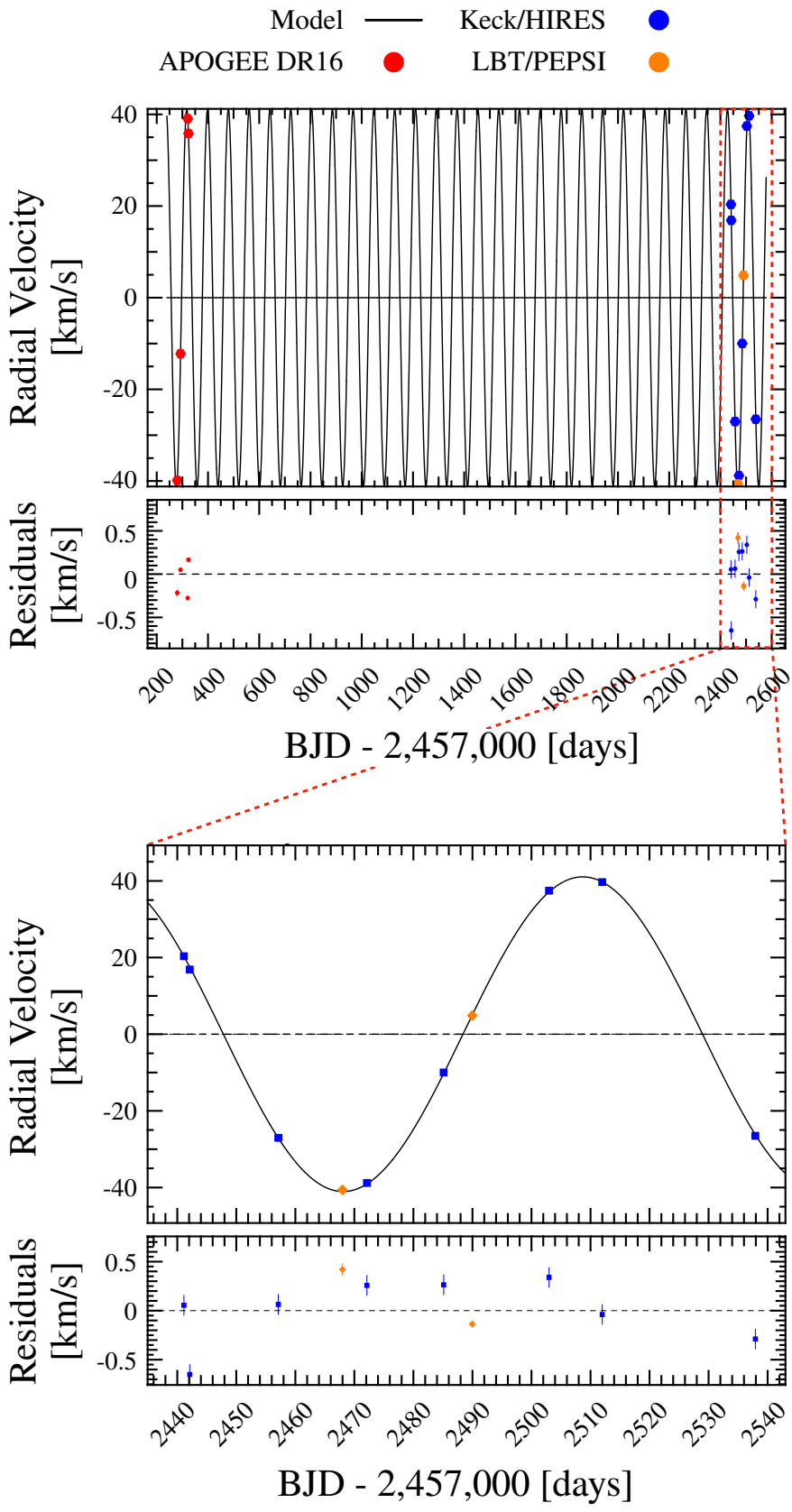

Figure 5. YORBIT radial velocity fit to the APOGEE, HIRES and PEPSI data. The top figure shows the entire observational timespan. The bottom figure is zoomed into our follow-up measurements with HIRES and PEPSI, covering slightly more than one orbital period.

Table 5. Orbital Elements for 2M0412

Parameter	Joint RV data+ `TheJoker`	Joint RV data+ `TheJoker`	HIRES+ `TheJoker`	Joint RV data + `yorbit`
$P_{\rm orb}$ (d)	81.439 ± 0.001	81.120 ± 0.001	81.136 ± 0.103	81.1643 ± 0.0029
K (km s^{-1})	41.041 ± 0.138	40.976 ± 0.144	41.016 ± 0.138	41.038 ± 0.138
e	–	0.004 ± 0.003	–	–
ω (°)	0 (fixed)	341 ± 71	0 (fixed)	0 (fixed)
v_γ (km s^{-1})	−47.137 ± 0.108	−47.096 ± 0.173	−47.217 ± 0.098	−47.031 ± 0.082
$a_{\rm giant} \sin i$ ($R_\odot$)	65.846 ± 0.214	65.996 ± 0.359	65.840 ± 0.285	65.840 ± 0.285
$f(M)$ ($M_\odot$)	0.583 ± 0.006	0.578 ± 0.006	0.580 ± 0.006	0.581 ± 0.002

which we discuss in §4. This is why we do not consider even lower giant masses (and radii) in Table 6.

In summary, the `PHOEBE` models indicate that the orbital inclination of 2M0412 is in the range $\sim 39.5 - 47.8°$ depending on the radius of the giant. The giant is not quite Roche-filling. The companion to the red giant is fairly massive, with $M_{\rm comp} \simeq 2.1 - 3.6\ M_\odot$ for $R_{\rm giant} = 23 - 33\ R_\odot$. The inferred mass of the red giant ($M_{\rm giant} \simeq 0.35 - 0.81\ M_\odot$) is inconsistent with the single-star MIST evolutionary tracks in §3.1 and instead implies that it has been heavily stripped by binary interaction.

As our fiducial model for the remainder of the paper, we adopt the `PHOEBE` model that most closely matches all of the available data. This is the model in Table 6 that matches the SED radius of $R_{\rm giant} \simeq 29\ R_\odot$. The mass of the giant is $M_{\rm giant} = 0.595^{+0.002}_{-0.006}\ M_\odot$, and the binary mass ratio is $q = M_{\rm giant}/M_{\rm comp} = 0.1995^{+0.0010}_{-0.0010}$. The orbital inclination is $i_{\rm orb} = 41.91^{+0.12\,\circ}_{-0.10}$, consistent with the estimates from $v_{\rm rot} \sin i$ (§3.1). In this model, the giant nearly fills its Roche lobe with $f = R_{\rm giant}/R_{\rm Roche} \simeq 0.97$. This model is a good fit to the ZTF r-band, the *TESS* T-band light curve, and the radial velocities (Figure 6). In this fiducial model, the companion mass is $M_{\rm comp} = 2.972^{+0.017}_{-0.015}\ M_\odot$, which implies a mass gap compact object if the companion is non-stellar. The companion mass exceeds both main sequence and subgiant single-star and binary-star limits from the SED (§3.1, Fig. 3). A complete discussion of all of the constraints on the companion is provided in §4.

3.4 A second component in the RV cross-correlation function?

The automated SB2 analysis tool `reamatch` (Kolbl et al. 2015) in the Keck CPS pipeline is used to identify double-lined spectroscopic binaries. It finds a secondary peak in the radial velocity cross-correlation function (CCF) for 2M0412 in most of the HIRES spectra (see Figure 7). `reamatch` only reports an approximate velocity for the second component. To derive more precise estimates, we use `iSpec` to derive RVs for this second component for both the HIRES and PEPSI epochs by cross-correlating the spectra with a synthetic spectrum generated with the atmospheric parameters in Table 4. `reamatch` also provides estimates of the secondary temperature and the relative brightness of the secondary in the V/R-bands. The secondary temperature is estimated to be $T_{\rm eff,comp} \sim 6000 - 6100$ K, which lies at the edge of the `reamatch` grid. The relative brightness of the secondary is estimated to range from ∼20% to ∼75%. These estimates significantly exceed the veiling fluxes that we estimated in §3.3 (V: ∼13%, R: ∼7%). However, Kolbl et al. (2015) noted that `reamatch` overestimated the relative brightness of hotter, secondary stars, and given that the template used to estimate the parameters of the secondary lies at the very edge of their library, we do not view the `reamatch` parameter estimates as being accurate.

Figure 8 shows the radial velocities for the secondary component after subtracting the systemic velocity v_γ. If we fix the period and orbital phases based on the orbit of the giant, we find a good fit (see Figure 8) to these velocities with $K_{\rm comp} = 8.3 \pm 0.1$ km s^{-1}, which implies $q = M_{\rm giant}/M_{\rm comp} = 0.201 \pm 0.010$ and $a_{\rm comp} \sin i = 13.3 \pm 0.2\ R_\odot$. This agrees very well with the mass ratio derived from our fiducial `PHOEBE` model (see §3.3 and the $R_{\rm giant} = 29\,{\rm R}_\odot$ column in Table 6). This estimate is also consistent with that obtained from Equation 3.

Using just the dynamical information ($K_{\rm giant}$, $K_{\rm comp}$ and $P_{\rm orb}$), we get $a_{\rm orb} \sin i = (a_{\rm giant} + a_{\rm comp}) \sin i = 80.4 \pm 0.2\ R_\odot$. Using Kepler's third law, this corresponds to $M_{\rm tot} \sin^3 i = (M_{\rm giant} + M_{\rm comp}) \sin^3 i = 1.06 \pm 0.01\ M_\odot$. Using the constraint on q, we can derive the minimum mass of the companion and the giant as

$$M_{\rm comp} \sin^3 i = 0.88 \pm 0.01\ M_\odot, \tag{4}$$

and

$$M_{\rm giant} \sin^3 i = 0.18 \pm 0.01\ M_\odot. \tag{5}$$

For the giant to have the minimum mass given its luminosity, $M_{\rm giant} = M_{\rm core} \simeq 0.32\ M_\odot$ (Equation 9), $\sin i = 0.83 \pm 0.01$ and $i = 55.6 \pm 1.0°$. At this inclination, $M_{\rm comp} = 1.6 \pm 0.1\ M_\odot$, which is again larger than the single star main sequence limit from the SED ($M_* \gtrsim 1.4\ M_\odot$ for MS stars). When compared to the `PHOEBE` fits shown in Table 6, a binary model with $M_{\rm giant} = M_{\rm core} \simeq 0.32\ M_\odot$ would have a giant radius $R_{\rm giant} \lesssim 23\ R_\odot$ and a distance $d \lesssim 3.2$ kpc, which is inconsistent with the observations.

To investigate the second component further, we subtract the best-fit synthetic spectrum of the giant from the HIRES spectra and shift the residuals to the companion's rest-frame. We then calculate the median spectrum from these residuals. As seen in Figure 9, the median of these residual spectra shows absorption features. If we fit the spectrum with `iSpec` keeping [M/H] fixed at the metallicity of the giant (§3.1), we find $T_{\rm eff,comp} = 6347 \pm 700$ K, $\log(g) = 3.1 \pm 0.2$, $[\alpha/{\rm Fe}] = 0.00 \pm 0.08$, and $v_{\rm rot} \sin i = 17.6 \pm 0.6$ km s^{-1}. As shown in Figure 9, this model fits the absorption features extremely well. For $i = 44°$, $v_{\rm rot} \simeq 25$ km s^{-1}. A main sequence star with $T_{\rm eff,comp} \simeq 6400$ K has a mass of $\sim 1.3\ M_\odot$, which is just below the single star SED limit of $M_* \lesssim 1.4\ M_\odot$ ($M_* \lesssim 1.7\ M_\odot$ for subgiants). However, a single star with $\sim 1.3\ M_\odot$ cannot account for the mass of the component implied by our constraint on q unless the giant mass is $M_{\rm giant} \simeq 0.26\ M_\odot$. Additionally, a $\sim 1.3\ M_\odot$ main sequence star cannot exist in a binary with a $\sim 1.1\ M_\odot$ red giant without a history of binary interaction.

While making the companion a binary with a compact object would solve this missing mass problem, the radial velocities would then be dominated by the motion of this inner binary and so we would not observe what seems to be the reflex motion of the outer binary. This would be true even for a binary comprised of two stars. For exam-

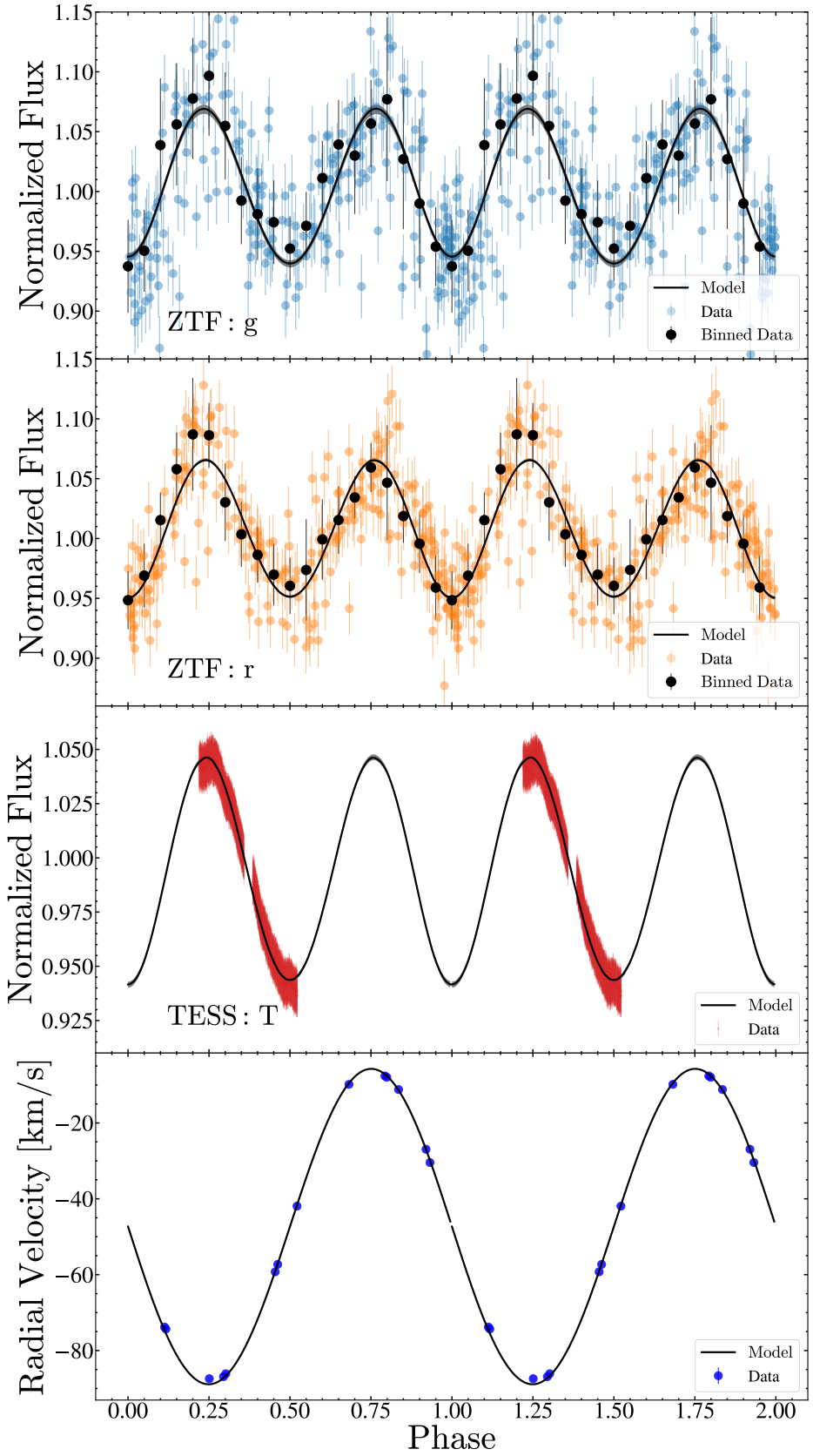

Figure 6. The normalized ZTF g, ZTF r and TESS T-band light curves for 2M0412 as a function of orbital phase (defined with the epoch of maximal RV at $\phi = 0.75$). The binned light curves for the ZTF g and ZTF $r-$ band light curves are shown as black points. The scatter in the bins are shown as errorbars. The light curves from the fiducial PHOEBE model for a giant + compact object binary with $R_{\rm giant} = 29\ R_{\odot}$ are also shown.

Table 6. Summary of the orbital and component parameters from the PHOEBE models for a giant + compact object binary at fixed radii. We assumed a circular orbit with $P_{\rm orb}$ = 81.16839 d and $a_{\rm giant} \sin i$ = 67.103 $R_\odot$ with the temperature of the giant fixed at to $T_{\rm eff,giant}$ = 4200 K. The reported errors are purely statistical and do not include systematic effects.

Parameter	R = 23 $R_\odot$	R = 25 $R_\odot$	R = 27 $R_\odot$	R = 29 $R_\odot$	R = 31 $R_\odot$	R = 33 $R_\odot$
d (kpc)	3.2	3.5	3.8	4.1	4.4	4.7
$i_{\rm orb}$ (°)	$47.82^{+0.10}_{-0.10}$	$46.34^{+0.14}_{-0.12}$	$44.40^{+0.11}_{-0.11}$	$41.91^{+0.12}_{-0.10}$	$40.58^{+0.11}_{-0.10}$	$39.51^{+0.11}_{-0.10}$
$q_{\rm orb}$	$0.1699^{+0.0010}_{-0.0011}$	$0.1881^{+0.0011}_{-0.0011}$	$0.1983^{+0.0009}_{-0.0008}$	$0.1995^{+0.0010}_{-0.0010}$	$0.2112^{+0.0009}_{-0.0009}$	$0.2251^{+0.0008}_{-0.0008}$
$v_{\rm rot} \sin i$ (km s^{-1})	$10.6^{+0.1}_{-0.1}$	$11.3^{+0.1}_{-0.1}$	$11.8^{+0.1}_{-0.1}$	$12.1^{+0.1}_{-0.1}$	$12.6^{+0.1}_{-0.1}$	$13.1^{+0.1}_{-0.1}$
$\log(g)$	$1.28^{+0.01}_{-0.01}$	$1.28^{+0.01}_{-0.01}$	$1.29^{+0.01}_{-0.01}$	$1.29^{+0.01}_{-0.01}$	$1.30^{+0.01}_{-0.01}$	$1.31^{+0.01}_{-0.01}$
$f = R_{\rm giant}/R_{\rm Roche}$	0.90	0.92	0.94	0.96	0.97	0.98
$M_{\rm giant}$ ($M_\odot$)	$0.351^{+0.038}_{-0.051}$	$0.432^{+0.003}_{-0.003}$	$0.511^{+0.002}_{-0.002}$	$0.595^{+0.002}_{-0.006}$	$0.693^{+0.002}_{-0.002}$	$0.807^{+0.002}_{-0.002}$
$M_{\rm comp}$ ($M_\odot$)	$2.071^{+0.005}_{-0.011}$	$2.294^{+0.012}_{-0.013}$	$2.579^{+0.013}_{-0.013}$	$2.972^{+0.017}_{-0.015}$	$3.280^{+0.016}_{-0.019}$	$3.586^{+0.012}_{-0.019}$
$a_{\rm orb}$ ($R_\odot$)	$106.0^{+0.1}_{-0.2}$	$110.2^{+0.2}_{-0.2}$	$114.9^{+0.2}_{-0.2}$	$120.5^{+0.2}_{-0.2}$	$125.0^{+0.2}_{-0.2}$	$129.2^{+0.2}_{-0.2}$
$a_{\rm comp}$ ($R_\odot$)	$15.4^{+0.1}_{-0.1}$	$17.5^{+0.1}_{-0.1}$	$19.0^{+0.1}_{-0.1}$	$20.1^{+0.1}_{-0.1}$	$21.8^{+0.1}_{-0.1}$	$23.7^{+0.1}_{-0.1}$
$a_{\rm RG}$ ($R_\odot$)	$90.6^{+0.2}_{-0.2}$	$92.8^{+0.2}_{-0.2}$	$95.9^{+0.2}_{-0.2}$	$100.5^{+0.2}_{-0.2}$	$103.2^{+0.2}_{-0.2}$	$105.5^{+0.2}_{-0.2}$

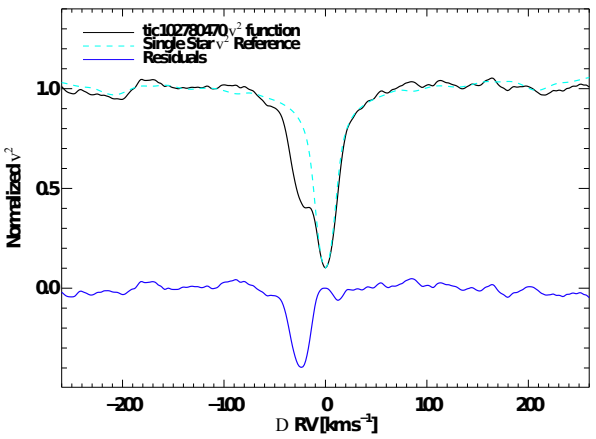

Figure 7. χ^2 as a function of the Doppler shift for the HIRES epoch at phase 0.92. The black line shows the observed reamatch χ^2 function (Kolbl et al. 2015) for 2M0412. The light blue dashed line shows the expected χ^2 function for a single star. The dark blue line shows the residual χ^2 function after subtracting the single star reference.

ple, an equal mass binary consisting of two 1.3 $M_\odot$ stars with a separation $a_{\rm comp}$ = 30 $R_\odot$ will have an orbital period of ∼11.8 days. The velocity of each component in this binary is ∼64 km s^{-1} (∼41 km s^{-1}) for i = 90° (i = 40°), which exceeds the reflex motion (∼8 km s^{-1}) and the broadening ($v_{\rm rot} \sin i$∼18 km s^{-1}) observed in the secondary absorption lines. All other configurations of equal mass inner binaries will have shorter orbits and therefore, larger velocities.

To investigate the scenario of a giant + star binary with `PHOEBE`, we fit the RVs of the second component along with the RVs of the giant, the ZTF r-band + g-band light curve, and the *TESS* T-band light curve. Instead of a compact object companion, we fit for the radius and temperature of a luminous companion star. We used a prior on the temperature based on the spectral fits ($T_{\rm eff,comp}$ = 6347±700 K). For this model, we obtained $M_{\rm giant} = 0.626^{+0.054}_{-0.049}$ $M_\odot$, $M_{\rm comp} = 2.72^{+0.18}_{-0.18}$ $M_\odot$, $R_{\rm giant} = 30.8^{+0.9}_{-0.9}$ $R_\odot$, $R_{\rm comp} = 8.8^{+1.2}_{-0.9}$ $R_\odot$, $T_{\rm eff,giant} = 4240^{+110}_{-140}$ K, $T_{\rm eff,comp} = 5950^{+170}_{-290}$ K, $i = 44.4^{+1.4}_{-1.1}$°, and $q = M_{\rm giant}/M_{\rm comp} = 0.232^{+0.007}_{-0.007}$. This model has $\log(g) = 3.0 \pm 0.1$ for the companion, consistent with the results from fitting the spectra. However, the companion is fairly large and luminous, with $L_{\rm comp} \simeq 87\ L_\odot$. In the g, r and *TESS* bands, the companion contributes ∼43%, ∼31% and ∼27% of the total luminosity, respectively. Such a star is inconsistent with the observed SED (§3.1).

Figure 10 shows the position of this companion in $\log(g)$ vs. $T_{\rm eff}$ as compared to a sample of APOGEE DR16 stars. If we search for stars similar to the `PHOEBE` companion in APOGEE DR16, we find 69 stars with 2.5 ≤ $\log(g)$ ≤ 3.5, 5600 K ≤ $T_{\rm eff}$ ≤ 6400 K and `ASPCAPFLAG`=0. To estimate their radii, we cross-match this list the TESS Input Catalog (TIC) and select 50 sources with radius measurements and distances < 3 kpc. The 16$^{\rm th}$,50$^{\rm th}$ and 84$^{\rm th}$ percentile of their radii and luminosity are $R_* = 4.1^{+2.3}_{-2.5}$ $R_\odot$ and $L_* = 16^{+23}_{-14}$ $L_\odot$.

Another explanation for the second set of absorption lines is that it emerges from an accretion disk/flow surrounding a compact object. In §3.5, we show that the source has a broad, double-peaked Hα emission line in our spectra, and argue that it likely emerges due to an accretion disk. While absorption lines are rarely seen in the spectra of accretion disks, it is not unprecedented. For example, Strader et al. (2016) identified two sets of absorption lines in spectra of the neutron star X-ray binary 3FGL J0427.9−6704, which corresponded to the stellar component and the accretion disk. The second set of absorption lines track the reflex motion of the neutron star primary and also matched the velocities derived from the emission features associated with the accretion disk.

Using `ELC` we tried fitting the ZTF g, r and *TESS* light curves along with the radial velocities of the giant and the second component as a star plus a compact object with an accretion disk. We retain the priors from the ELC fits described in §3.3, but in this model we keep the temperature of the giant fixed at $T_{\rm eff,giant}$ = 4150 K. For the disk, we fit the inner $r_{\rm in}$ and outer radii $r_{\rm out}$ in units of

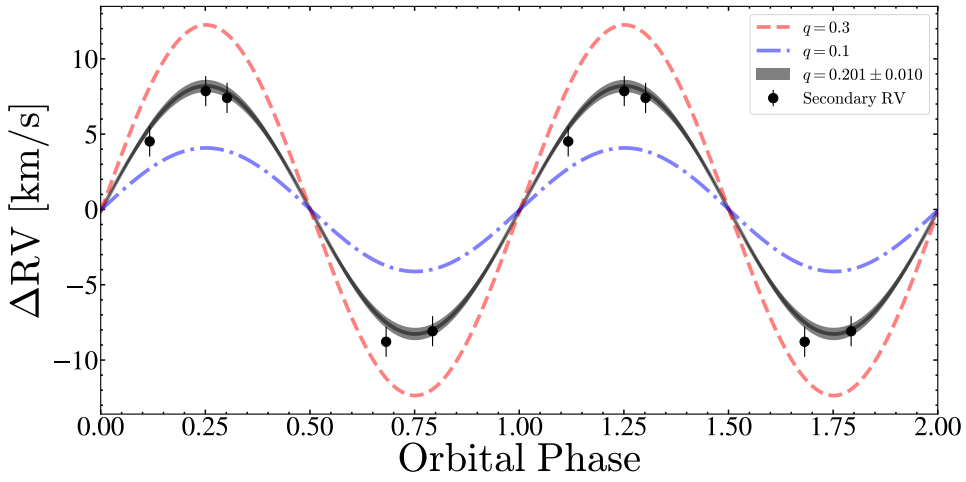

Figure 8. Orbital velocity as a function of phase for the second component in the HIRES and PEPSI spectra. The black shaded region illustrates the expected counter-motion of a component with a mass ratio $q = 0.201 \pm 0.010$. Theoretical RV curves for mass ratios of $q = 0.3$ and $q = 0.1$ are shown as red dashed and blue dot-dashed lines respectively.

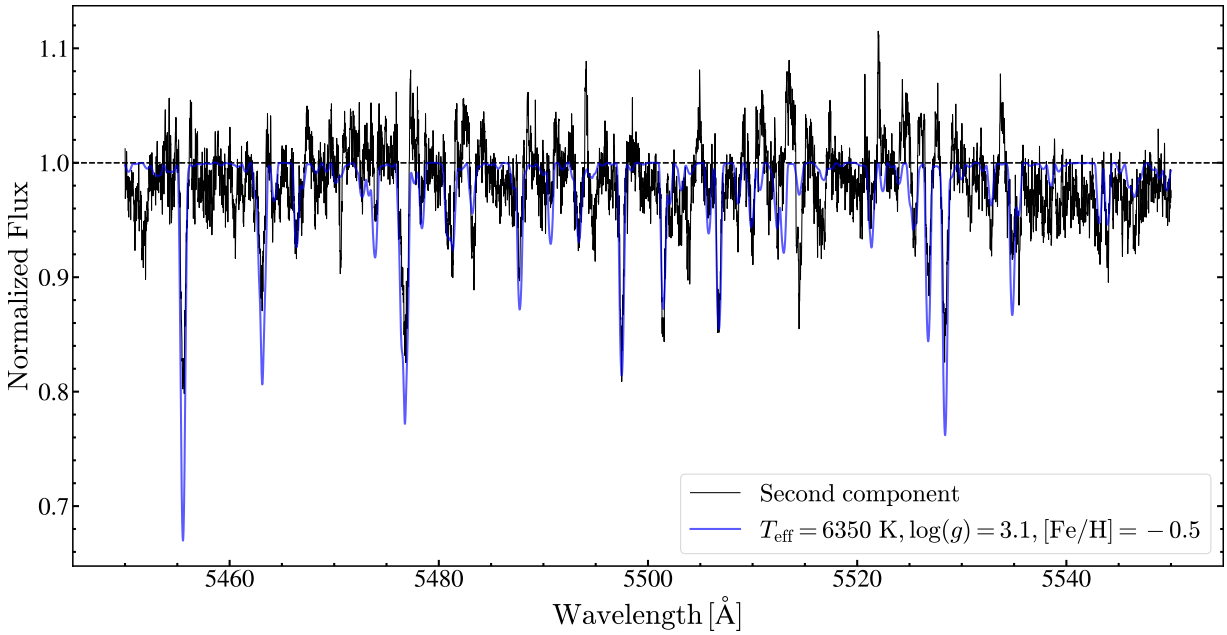

Figure 9. The median spectrum of the second component from 5450 Å to 5550 Å (black) in its rest frame after subtracting the synthetic spectrum of the giant from the HIRES spectra. Model spectra for a star at the giant's metallicity with $T_{\rm eff} = 6350$ K and $\log_(g) = 3.1$ is shown in blue.

the Roche radius of the compact object $r_{\rm RL}$, the temperature $T_{\rm in}$ of the disk at $r_{\rm in}$, the power-law exponent on the temperature profile of the disk $T(r) \propto T_{\rm in}(r/r_{\rm in})^{\xi}$, and the opening angle of the disk rim above the plane β. We find $M_{\rm giant} = 0.72^{+0.04}_{-0.03}$ $M_\odot$, $M_{\rm comp} = 3.11^{+0.11}_{-0.08}$ $M_\odot$, $R_{\rm giant} = 32.2^{+0.6}_{-0.5}$ $R_\odot$, $i = 42.4^{+0.5}_{-0.6}{}^\circ$, and $q = M_{\rm giant}/M_{\rm comp} = 0.184^{+0.041}_{-0.079}$. For the disk, we obtain $r_{\rm in}/r_{\rm RL} = 0.020^{+0.019}_{-0.014}$, $r_{\rm out}/r_{\rm RL} = 0.819^{+0.126}_{-0.135}$, $T_{\rm in} = 9000^{+7100}_{-1600}$ K, $\xi = -0.52^{+0.06}_{-0.12}$, and $\beta = 30.3^{+15.0}_{-23.6}{}^\circ$. This model is, however, a slightly worse fit than the ELC models without any emission from the companion. In physical units the disk spans from $r_{\rm in} \simeq 1.3$ $R_\odot$ to $r_{\rm out} \simeq 51.4$ $R_\odot$ compared to a Roche limit for the secondary of $r_{\rm RL} \simeq 62.8$ $R_\odot$. While the origin of absorption lines from a disk remains an issue, the temperatures of the disk in the inner regions of this model are not in gross conflict with the model of the spectrum.

The presence of the secondary RV component raises an interesting dilemma. Given the expected mass of the giant from our PHOEBE model in §3.3 ($M_{\rm giant} \simeq 0.6$ $M_\odot$), the mass ratio required by the radial velocities require $M_{\rm comp} \simeq 3.0$ $M_\odot$, entirely consistent with the estimate from PHOEBE. However, a stellar companion with this mass would be trivially visible in the SED (Figure 3), especially towards the UV. For example, a ~3.0 $M_\odot$ main sequence B star with a temperature of ~11, 000 K and a luminosity ~100 $L_\odot$ can be easily ruled out.

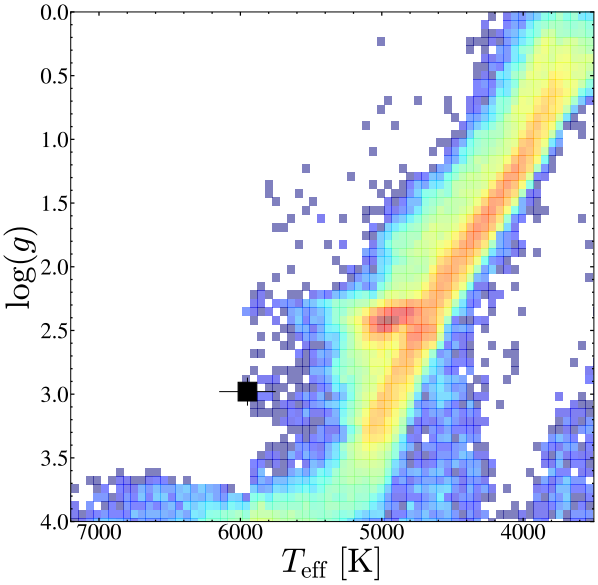

Figure 10. $\log(g)$ vs. $T_{\rm eff}$ for the sample of APOGEE DR16 giants. The estimated position of the second component is shown in black.

3.5 Balmer Hα emission

As shown in Figure 11, there is a broad Hα emission line whose structure varies with the orbital phase. V723 Mon also has this property (Jayasinghe et al. 2021b), but here it is directly visible without any need to subtract the stellar spectrum.

We identify both blue-shifted and red-shifted emission components in most of our spectra. We define these components by the wavelength ranges of 6560 – 6562 Å and 6564 – 6566 Å respectively. The most significant Hα emission in our spectra is seen near phase ϕ~0.9 as a blue-shifted component. The emission component has a velocity close to the rest frame of the giant near phase ϕ~0.25 and fills in the giant's Hα absorption line. Near phase ~0.9, the typical Gaussian FWHM of the blue-shifted (red-shifted) Hα emission component is ~255 km s^{-1} (~265 km s^{-1}). The wings of the emission extends beyond ~200 km s^{-1} in some of our spectra.

The peak separations at ϕ~0.1 and ϕ~0.9 are ~160 km s^{-1} and ~196 km s^{-1} respectively. However, the behavior of the double-peaked profile appears to vary between orbits. For example, we obtained Keck/HIRES spectra near ϕ~0.1 in two consecutive orbits, where the first spectrum has a peak separation of ~106 km s^{-1} and the second spectrum has a much larger peak separation of ~160 km s^{-1}. For the epochs where we can see a double-peaked emission profile, the median peak separation is ~168 km s^{-1} with a scatter of σ~31 km s^{-1}. The orbital phase evolution and profile morphology of the Hα emission is qualitatively similar to that seen in the red giant + neutron star binary 1FGL J1417.7−4407 (Strader et al. 2015).

Figure 12 shows the Hα line at various orbital phases along with the PHOEBE models of the orbital configurations of the binary. After conjunction at $\phi \simeq 0.5$, the emission is blue-shifted and reaches a maximum at phase ϕ~0/1 (Figure 14). Since the Hα emission varies significantly in the rest-frame of the giant, this emission must emerge from beyond the giant's photosphere. Given its large FWHM, we can rule out a chromospheric origin for the Hα emission. We also do not observe the Ca II H and K emission lines that are typically associated with chromospheric activity,

Figure 13 shows the Hα line profiles after subtracting the template spectrum of the red giant. We see a blue-shifted Hα absorption feature in these line profiles at a roughly constant ~30 km s^{-1} blue shift relative to the giant. The depth of the absorption core is strongest near ϕ~0.5. The velocity of this absorption feature is close to the velocity of the giant's photosphere ($v_{\rm rot,giant} \simeq 20$ km s^{-1}), consistent with mass outflow from the giant at L_1. At $\phi = 0$, the inner Lagrangian point (L_1) is directed toward the observer and at $\phi = 0.5$, L_1 points away from the observer (Beech 1985). It is possible that the absorption feature is associated with density enhancements caused by matter streaming through the inner Lagrangian point.

Figure 14 shows how the equivalent width varies with orbital phase for both the blue-shifted and red-shifted Hα components. The largest equivalent width of the blue-shifted (red-shifted) Hα component is EW(Hα)~−0.5 (EW(Hα)~−0.3) at ϕ~0.9. These equivalent widths are more than an order of magnitude smaller than those observed for X-ray binaries (see, for e.g., Fender et al. 2009) and correspond to a total line luminosity of ~0.003 $L_\odot$. For both the blue and red components, the equivalent widths are the most negative (emission is strongest) near ϕ~0 when the companion is on the near side of the giant. The red-shifted line also has a weaker peak at ϕ~0.5 when the companion is on the far side. We are unable to do a similar analysis for the Hβ line because it is not included in the HIRES spectra and the PEPSI S/N is poor at Hβ.

If we interpret the double peaked structure as an accretion disk, the projected radial velocity of the outer rim of an accretion disk is approximately equivalent to half the velocity separation of the two peaks V_h (see, for e.g., Smak 1981; Strader et al. 2015). In this case, the V_h of 84 km s^{-1} is significantly larger than the radial velocity semi-amplitude of the red giant (~42 km s^{-1}). It is also slightly larger than the circular velocity at the surface of the giant (~78 km s^{-1} for $M = 1\ M_\odot$ and $R = 31\ R_\odot$). Indeed, V_h is expected to be larger than the radial velocity semi-amplitude of the giant for classical Keplerian disks (see, for e.g., Paczynski 1977; Orosz et al. 1994). As an orbit around the secondary, this velocity corresponds to $\simeq 27\ M_{\rm comp} \sin^2 i\ R_\odot$ or $\simeq 11\ M_{\rm comp}\ R_\odot$ if we use a disk inclination of 40°.

In summary, we observe a phase dependent, broad ($\gtrsim$ 200 km s^{-1}) Hα emission line in our spectra of 2M0412. We show that the morphology and orbital evolution of the Hα emission is likely due to an accretion disk. This is consistent with our interpretation of this system where the red giant nearly fills its Roche lobe. However, more spectra are needed to study the behavior of the Hα emission in greater detail.

3.6 X-ray upper limit

No X-rays were detected in the *Swift* XRT observations. We derived a 3 sigma upperlimit using the reprocessed observations of sw00014417001 (~2.2 ks), a 50 arcsec source region centered on the source and a 150 arcsec source free background region located at ($\alpha_{J2000}, \delta_{J2000}$)=(04:12:38.10,67:43:00.86). We derive an aperture corrected 3σ upper limit on the 0.3-2.0 keV count rate of 8.1×10^{-4} counts/s. Using the Galactic column density along the line of sight ($N_H \sim 1.34 \times 10^{22}$ cm^{-2}, HI4PI Collaboration et al. 2016), and an absorbed power-law with a photon index of 2, we derive an absorbed (unabsorbed) flux of 1.7×10^{-14} erg cm^{-2} s^{-1} (5.0×10^{-14} erg cm^{-2} s^{-1}), which corresponds to an absorbed (unabsorbed) X-ray luminosity of 3.4×10^{31} erg s^{-1} (9.5×10^{31} erg s^{-1}). The *Swift* XRT upper limit is compatible with the X-ray luminosities expected of quiescent X-ray binaries ($L_{\rm X} \sim 10^{30} - 10^{31}$ ergs s^{-1}; Dinçer et al. 2018). If the X-ray luminosity originates from an accretion disk around a ~3.0 $M_\odot$ black hole, the luminosity is $\lesssim 1.1 \times 10^{-7}\ L_{\rm edd}$.

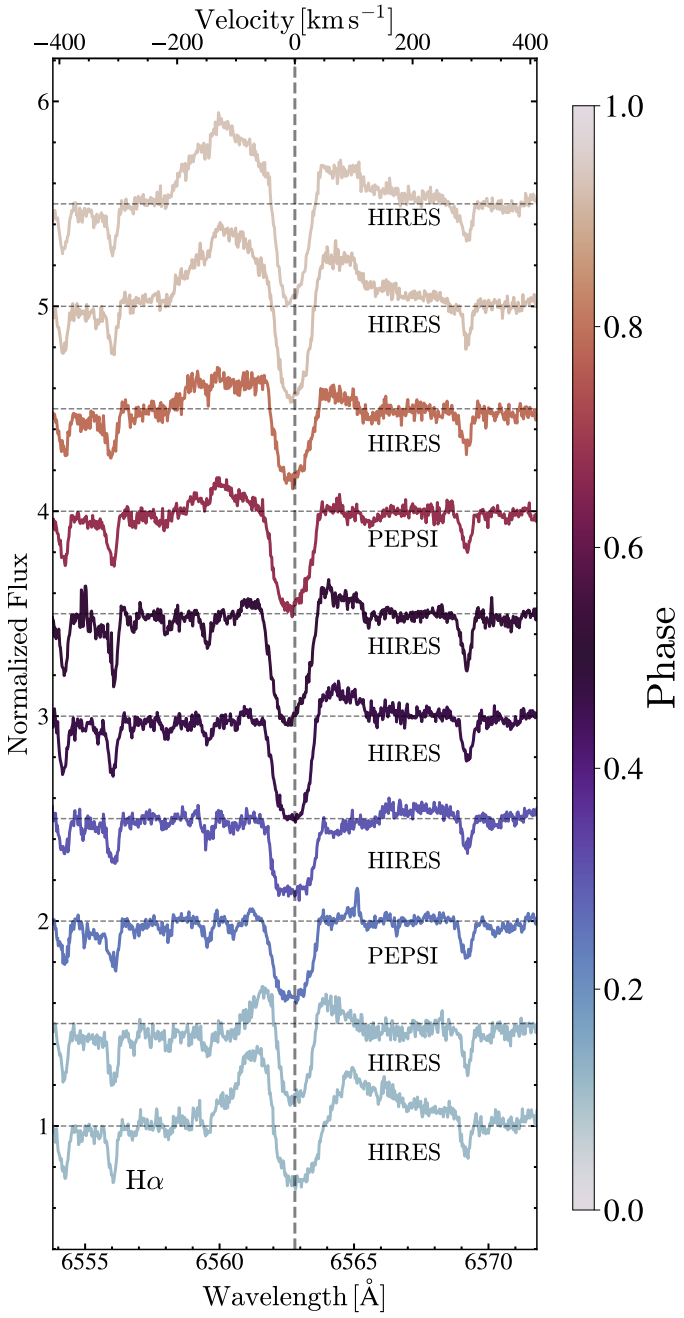

Figure 11. Hα line profiles in the rest frame of the giant in the HIRES and PEPSI spectra. The line profiles are sorted and colored as a function of orbital phase.

We estimate the mass loss rate from the giant as

$$\dot{M} = 4 \times 10^{-13}\, \eta_R\, \frac{LR}{M}\, M_\odot \mathrm{yr}^{-1} \approx 2 \times 10^{-9}\, M_\odot \mathrm{yr}^{-1}, \quad (6)$$

(Reimers 1975) where L, R and M are in solar units and $\eta_R \simeq 0.477$ (McDonald & Zijlstra 2015). The velocity of the wind from the giant is assumed to be the escape velocity, $V_{\rm wind} \approx V_{\rm esc} \sim 90\,\mathrm{km\ s}^{-1}$. For a scenario with wind-fed accretion to the compact object, Thompson et al. (2019) approximated the amount of material gathered at the

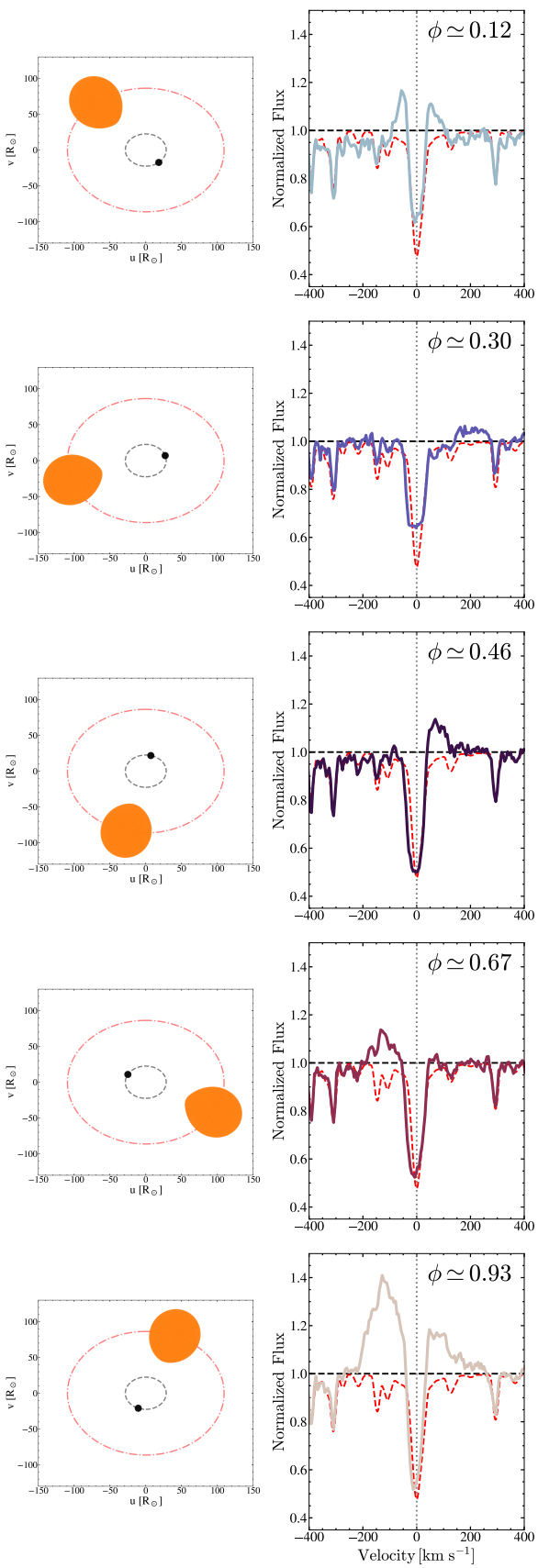

Figure 12. Behavior of the Hα line profiles with orbital phase. The right panels show the Hα line profiles at the orbital configurations illustrated in the left panels. The size of the companion is simply chosen to make it easily visible. The red dashed line shows the best fit synthetic spectrum for the giant.

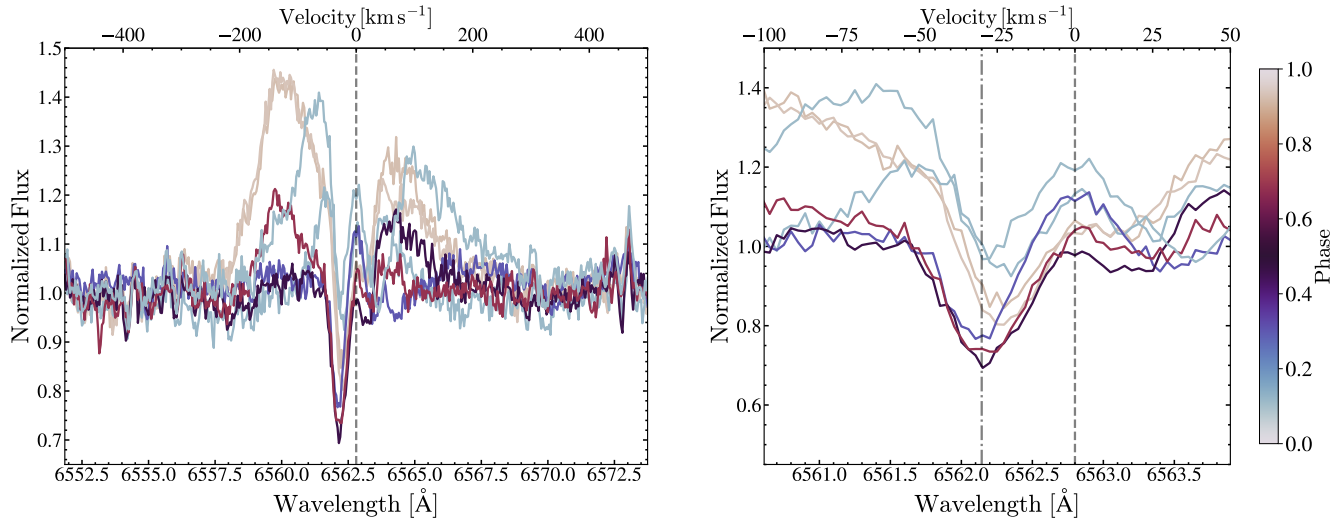

Figure 13. Variations of the Hα line profiles with orbital phase in the giant's rest frame after subtracting a template spectrum for the red giant. The left panel shows the full wavelength range and the right panel zooms in on the line core. Note the Hα absorption feature at $\simeq -30\,\mathrm{km\,s^{-1}}$ in the giant's rest-frame.

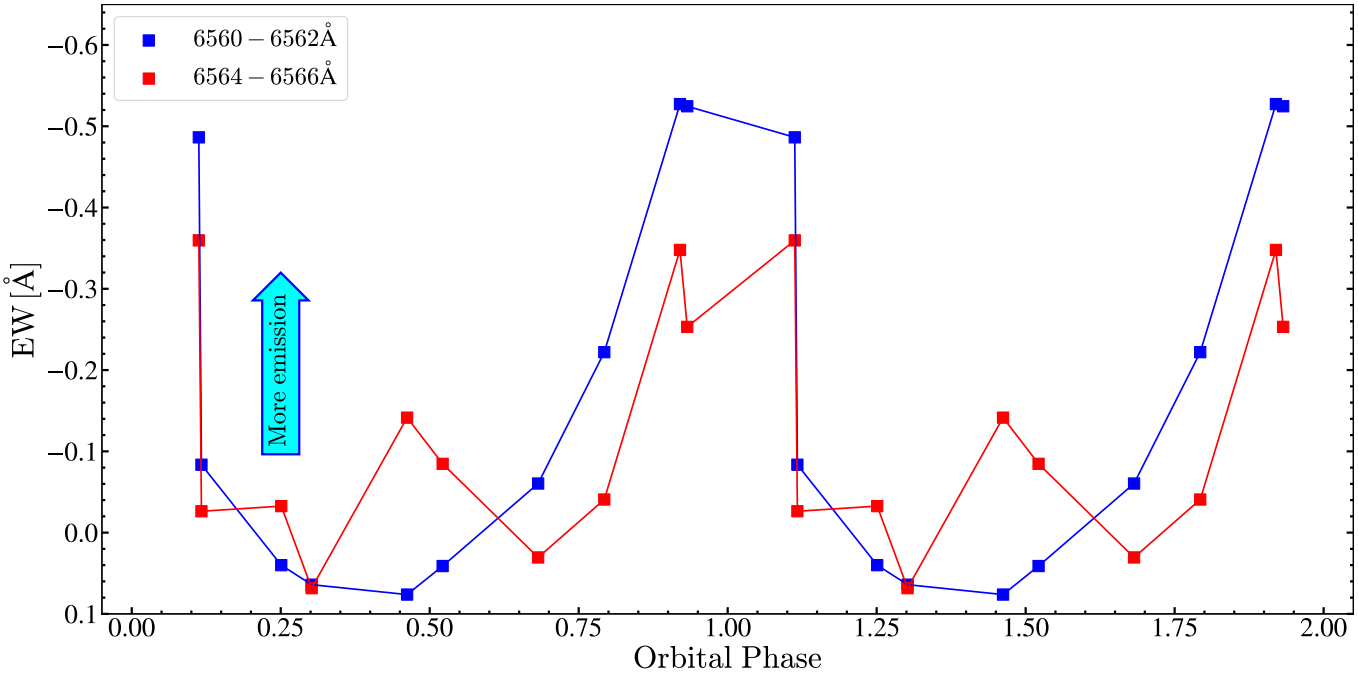

Figure 14. Equivalent width of the blue-shifted (blue points, 6560 – 6562 Å) and red-shifted (red points, 6564 – 6566 Å) Hα emission components as a function of orbital phase.

sphere of influence of the black hole as

$$\dot{M}_{\rm acc} \sim \frac{\pi \dot{M}}{(4\pi a_{\rm giant}^2)} \left(\frac{G M_{\rm BH}}{V_{\rm wind}^2}\right)^2 \sim 7\times10^{-11}\,{\rm M_\odot\ yr^{-1}}\ \dot{M}_{-9}\left(\frac{M_{\rm BH}}{3M_\odot}\right)^2\left(\frac{V_{\rm wind}}{120\,{\rm km\ s^{-1}}}\right)^{-4} \sim 4\times10^{-10}\,{\rm M_\odot\ yr^{-1}}, \quad (7)$$

where $\dot{M}_{-9} = \dot{M}/10^{-9}\,{\rm M_\odot\ yr^{-1}}$. For radiatively efficient accretion, the luminosity would be

$$L_{\rm acc} \sim 0.1\ \dot{M}_{\rm acc}\ c^2 \simeq 630\ L_\odot \simeq 7\times10^{-3}\ L_{\rm Edd}. \quad (8)$$

This estimate of the accretion luminosity is much larger than the observed X-ray luminosity of this system ($\lesssim 0.01\ L_\odot$) but for radiatively inefficient accretion, the luminosity can be much lower (Narayan & Yi 1995).

4 THE NATURE OF THE COMPANION

In this section, we systematically discuss the nature of the companion given the observed properties of the system and the modeling results from §3.

Figure 15 summarizes the overall landscape of the constraints on the masses of the giant and the companion. In all scenarios, the models have mass ratios q~0.2 and inclinations of $i = 40°$ to $50°$. The `PHOEBE` models at fixed radii of $R_{\rm giant}$ = 23, 25, 27, 29, 31, 33, and 35$R_\odot$ are marked (black symbols; see Table 6). Solid red lines show $q = 0.2$ and $q = 0.3$ for reference. That the companion RV signal in Figure 8 corresponds to a simple reflex motion of the giant and the associated absorption features are narrow rules out the possibility that the companion is a binary containing a star, so we focus on a system where the companion is a single star or compact object. The limits on the SED imply that if the companion is a single star, its maximum mass is $1.7M_\odot$, which requires a companion just evolving off the main sequence onto the sub-giant branch. If it is still on the main sequence, it must be less massive than $1.4M_\odot$, and this limit is shown in Figure 3 and the green hatched region in Figure 15.

We are unable to find any consistent explanation where the companion is a single star. Assuming the inclination and mass ratio are well-constrained, the only way to have a low mass companion that is sufficiently faint enough to remain undetected in the SED is by significantly reducing the distance, while simultaneously increasing the mass ratio to $q \simeq 0.3$ despite the multiple lines of evidence for $q \simeq 0.2$ and for a distance of $\simeq$ 4 kpc. In any such a scenario, the observed giant has lost a significant fraction of its envelope. Additionally, the companion that has gained mass needs to be much less luminous than a star with its present-day mass.

There are several constraints on the giant mass that are independent of single star evolution models and that we show in Figure 15. First, the giant is on the upper RGB and not on the red clump (Figure 4), so it has a degenerate core. The luminosity of a solar metallicity giant with a degenerate core of mass $M_{\rm core}$ is (Boothroyd & Sackmann 1988),

$$\left(\frac{L}{L_\odot}\right) \approx 1170\left(\frac{M_{\rm core}}{0.4\ M_\odot}\right)^7, \tag{9}$$

so we must have $M_{\rm giant} > M_{\rm core} \simeq 0.32\ M_\odot$ for $L \sim 230\ L_\odot$. The core mass–luminosity relationship is weakly dependent on metallicity. For example, this limit changes to $M_{\rm giant} > M_{\rm core} \simeq 0.34\ M_\odot$ for a metal-poor giant with $Z = 0.001$. This minimum mass sets the lowest mass PHOEBE model we considered in §3.3 and Table 6. This region is denoted by the orange hatched region in Figure 15. Second, the giant must lie inside its Roche limit. Using the Eggleton (1983) approximation for the Roche limit we illustrate the Roche radii for 25, 29, and 33 $R_\odot$ with the black dashed lines. We see in Figure 15 that the giant must be more massive than $M_{\rm giant} \gtrsim 0.5\ M_\odot$ for the radius of $R_{\rm giant} \simeq 29\ R_\odot$ from the SED (§3.1). Note that this limit is identical to the argument that the mean density of a Roche lobe-filling star is largely determined by the period (Eggleton 1983), which was recently used by El-Badry & Burdge (2021) in arguing against the NGC 1850 BH1 candidate discussed in the introduction. As discussed in §3.3, if the giant star is tidally locked, it cannot fully fill its Roche lobe (i.e. the Roche radius cannot be made consistent with the stellar radius needed for locking), so the star must lie to the right of these Roche limits and not lie exactly on them. Thus, we see from the 29 $R_\odot$ dashed line Figure 15, that if the giant is at least as large as 29 $R_\odot$ and is not completely filling its Roche lobe, $M_{\rm giant} \gtrsim 0.5\ M_\odot$ and the companion must have $M_{\rm comp} \gtrsim 1.7\ M_\odot$ for $q < 0.3$. For the preferred value of $q \simeq 0.2$ from the `PHOEBE` fits and the second RV component (Table 6, Figure 8), the giant's mass is $M_{\rm giant} \simeq 0.6\ M_\odot$ and the companion has $M_{\rm comp} \simeq 3\ M_\odot$. This model, which is most consistent with all of the observational constraints is shown as the large filled black pentagon in Figure 15.

Evading these limits requires making the star physically smaller. It does not seem feasible to do this by raising the temperature, which is well-constrained. The SED models and the models of the spectra are in excellent agreement on the temperature of the giant. If the temperature is known, the only way to reduce the stellar radius is to reduce the distance since for fixed temperature, $R_{\rm giant} \propto L_{\rm giant}^{1/2} \propto d$. We have used a distance of $d = 4.0$ kpc based on the parallax corrected for the global zero-point parallax offset in *Gaia* EDR3. Alternatively, Hogg et al. (2019) find a distance of $d = 4.4$ kpc using a spectrophotometric parallax, which is 10% larger, implying a larger $R_{\rm giant} \simeq 31\ R_\odot$, and thus a larger giant mass for consistency with the PHOEBE models (§3.3; Table 6). Alternatively, Bailer-Jones et al. (2021) find a distance of $d = 3.7$ kpc ($R_{\rm giant} \simeq 27\ R_\odot$), which is almost 8% smaller than our fiducial 4 kpc. The latter is derived using the zero-point offset corrections from Lindegren et al. (2021a), while consistent with the Bailer-Jones et al. (2021) distance, might be biased due to an over-correction of the zero-point parallax offset (see, for e.g., Groenewegen 2021; Bhardwaj et al. 2021; Zinn 2021). A smaller distance would reduce the radius to $R_{\rm giant} = 27\ R_\odot$ and the Roche limit would allow the giant to have a mass as low as $M_{\rm giant} \gtrsim 0.4\ M_\odot$, but would still indicate a companion mass of $\simeq 2\,M_\odot$ for $q = 0.2$. We note that that Bailer-Jones et al. (2021) method uses a prior that weights distances based on the expected numbers of stars without reference to the stellar type. Since giants have larger distances than dwarfs at fixed magnitude, a prior based on all stars will generally bias the distance estimates to a giant to be low. Reducing the distance also tightens the SED limits on any companion: in Figure 3, the SED of the giant moves downwards while the SEDs of possible companions are unchanged.

Finally, assuming tidal synchronization, we can also use $v_{\rm rot} \sin i$ to estimate the radius of the giant

$$R \sin i = 19.3\ R_\odot \left(\frac{v_{\rm rot} \sin i}{12\ {\rm km\ s^{-1}}}\right), \tag{10}$$

which gives $R_{\rm giant} = 38.5\ R_\odot, 29.9\ R_\odot, 25.1\ R_\odot$, and $22.2\ R_\odot$ for $i = 30°, 40°, 50°$, and $60°$. `isoclassify` single star evolution models based on the spectroscopic parameters and the photometry used in the SED model given an estimated mass of $M_{\rm giant} = 1.11^{+0.24}_{-0.22}\ M_\odot$ and a radius of $R_{\rm giant} = 29.8^{+2.2}_{-2.0}\ R_\odot$. The spectroscopic $\log g$ estimates give a mass of $M_{\rm giant} = 0.9 \pm 0.6 M_\odot$ that is consistent with any of these estimates.

4.1 Comparison to BPASS binary evolution models

As an initial experiment we used `hoki` (Stevance et al. 2020) to search for Binary Population And Spectral Synthesis (BPASS; Eldridge et al. 2017; Stanway & Eldridge 2018) binary models consistent with the observed properties of 2M0412. We used the BPASS v2.2.1 models at Z = 0.006, which is the closest match to the metallicity derived in §3.1.

We restrict our search to models with

(i) Period of the binary, $P_{\rm orb} = 81 \pm 8$ days,
(ii) $V = -0.61 \pm 1$ mag,
(iii) $J = -2.87 \pm 1$ mag,
(iv) $K = -3.68 \pm 1$ mag,
(v) Total luminosity of the binary, $\log(L_{\rm binary}) = 2.40 \pm 0.05$,
(vi) Radius of the giant, $\log(R_{\rm giant}) = 1.49 \pm 0.05$,

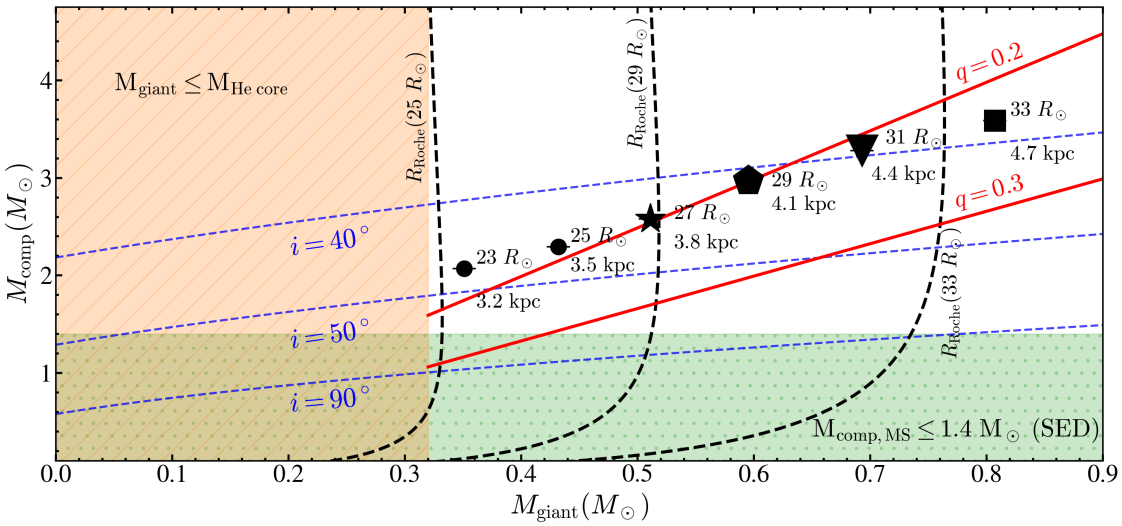

Figure 15. The mass of the companion ($M_{\rm comp}$) as a function of the mass of the giant ($M_{\rm giant}$). The binary mass function at inclinations of $i = 90°$, 40° and 30° are shown as the blue dashed lines. Giants with radii of $R = 25\ R_\odot$, $R = 29\ R_\odot$ or $R = 33\ R_\odot$ will overfill their Roche lobes of $R_{\rm Roche}(R)$ if they have masses less than the Roche limits given by the dashed curves. The companion masses for a mass ratio of $q = 0.2$ and $q = 0.3$ are shown as the red lines. The orange shaded region highlights giant masses that are not allowed by the condition $M_{\rm giant} \gtrsim M_{\rm core} \simeq 0.32\ M_\odot$ (Equation 9). The green shaded region shows companion masses for luminous stars that are allowed by the single star SED limit ($M_* \lesssim 1.4\ M_\odot$ for main sequence stars, §3.1, Figure 3). The SED limit of $M_* \lesssim 1.7\ M_\odot$ for subgiant stars is excluded for clarity. The derived values for $M_{\rm comp}$ and $M_{\rm giant}$ from the PHOEBE models at fixed giant radii (§3.3, Table 6) are shown in black.

(vii) Effective temperature of the giant, $\log(T_{\rm eff}) = 3.62 \pm 0.05$,
(viii) Mass of the giant, $M_{\rm giant} = [0.35, 2]\ M_\odot$, and
(ix) Binary mass ratio, $0.15 < q < 0.35$.

We searched for models where either (1) the companion is a star with an effective temperature lower than $T_{\rm eff,comp} < 7000$ K, or (2) the companion is a compact object. We found 11 giant + star and 19 giant + compact object models that satisfied these criteria. In all of the models, the giant is heavily stripped with masses in the range of $\sim 0.38 - 0.60\ M_\odot$ ($M_{\rm init} \simeq 1.4 - 2.3\ M_\odot$) and $\sim 0.36 - 0.79\ M_\odot$ ($M_{\rm init} \simeq 0.9 - 2.5\ M_\odot$) for the giant + star and the giant + compact object models, respectively. Table 7 gives the models closest in period and magnitude ($P_{\rm orb} = 81 \pm 2$ days, $\Delta(M) = 0.5$ mag) as examples.

The BPASS model that best matches our observations and derived properties is a giant + compact object binary. In this model, $M_{\rm giant} \simeq 0.78\ M_\odot$, $M_{\rm comp} \simeq 3.71\ M_\odot$, $q \simeq 0.21$, $R_{\rm giant} \simeq 30.6\ R_\odot$, $T_{\rm eff,giant} \simeq 4246$ K, $\Delta(V) = 0.09$ mag, $\Delta(J) = 0.04$ mag, and $\Delta(K) = 0.01$ mag. Given that Roche lobe overflow (RLOF) has now ceased, this binary will have a similar orbital configuration (period and semi-major axis) for ~173 Myr. Over a period of ~2 Myr, the giant lost ~69% of its pre-RLOF mass through RLOF. The three other giant + compact object binary models in Table 7 are still undergoing RLOF with total durations of ~5 – 21 Myr. Unlike the best match model, the other binaries are evolving rapidly as RLOF is still ongoing. In these three models, the giant ultimately loses ~57 – 77% of its initial mass.

The giant + star binary that best matches our data has $M_{\rm giant} \simeq 0.60\ M_\odot$, $M_{\rm comp} \simeq 2.15\ M_\odot$, $q \simeq 0.280$, $R_{\rm giant} \simeq 33.5\ R_\odot$, $T_{\rm eff,giant} \simeq 4039$ K, $\Delta(V) = 0.06$ mag, $\Delta(J) = 0.01$ mag, and $\Delta(K) = 0.14$ mag. Comparing this model with the best giant + compact object model, the current configuration of the giant + star binary is short-lived, with the orbit expanding to a period of ~102 days in ~1.4 Myr. In this model, the binary is undergoing RLOF with a total duration of ~13 Myr. The two other giant + star binary models in Table 7 have similar properties. In these models, the giant loses ~63 – 69% of its initial mass. For a conservative mass-transfer binary, the accretor is spun up and will therefore be rapidly rotating. The companion star to the giant is ~2.9 – 3.4 mag ($F_{\rm comp}/F_{\rm binary}$~4.2% – 6.7%) and ~3.6 – 4.1 mag ($F_{\rm comp}/F_{\rm binary}$~2.4% – 3.6%) fainter than the overall binary in the V and R bands, respectively. Based on the NUV limits, we only can only very weakly rule out such companions.

We were puzzled by (in particular) the low temperatures of the stellar companions in the BPASS models. The cause is that the present BPASS models only evolve one star at a time for reasons of speed (Eldridge & Stanway 2016). This can lead to misestimates of the properties of the accreting star (Eldridge, private comm.). To examine this, we evolved the BPASS giant + star binaries (Models 1-3, Table 7) using Modules for Experiments in Stellar Astrophysics (MESA Paxton et al. 2011, 2013, 2015, 2018, 2019). MESA computes Roche lobe radii in binary systems using the fit of Eggleton (1983), and the mass transfer rates in Roche lobe overflowing binary systems are determined following the prescription of Kolb & Ritter (1990). We adopt the explicit mass transfer calculation scheme in MESA. We use the initial component masses and orbital period ($P_{\rm orb,init} = 25.2$ days) from the BPASS models and examine their properties when the binary has a period of $P_{\rm orb}$~81 days. As in the BPASS models, the initially more massive component becomes a red giant with $M_{\rm giant} \simeq 0.57 - 0.65\ M_\odot$ and its companion is a main sequence star with $M_{\rm comp} \simeq 2.09 - 2.39\ M_\odot$. The giant's properties of $T_{\rm eff,giant} \simeq 4094 - 4103$ K, $R_{\rm giant} \simeq 28.7 - 30.2\ R_\odot$, $\log(g) \simeq 1.3$ and $L_{\rm giant} \simeq 209 - 232\ L_\odot$ are virtually identical to those of the observed star. For all three models, the giant is still in the process of transferring mass to its companion when it reaches this period. Once the mass transfer is complete, the binary is at an orbital period of $P_{\rm orb} \simeq 220 - 281$ days.

In the MESA models, however, the companion to the giant is a hot, luminous star with $T_{\rm eff,comp} \simeq 10800 - 11700$ K, $R_{\rm comp} \simeq$

Table 7. Properties of the BPASS models that match observations for 2M0412.

Model	$M_{\rm giant}$ ($M_\odot$)	$M_{\rm He\ core}$ ($M_\odot$)	$M_{\rm comp}$ ($M_\odot$)	q	$T_{\rm eff,giant}$ (K)	$T_{\rm eff,comp}$ (K)	$R_{\rm giant}$ ($R_\odot$)	$R_{\rm comp}$ ($R_\odot$)	$L_{\rm giant}$ ($L_\odot$)	$P_{\rm orb}$ (d)	Age Gyr
1	0.49	0.33	1.70	0.288	4036	6860	31.0	1.5	230	83.0	1.8
2	0.52	0.32	1.81	0.289	4034	6273	31.0	1.9	229	80.4	2.7
3	[a] 0.60	0.33	2.15	0.280	4039	6871	33.5	2.1	269	83.1	1.8
4	0.48	0.32	3.02	0.160	4073	–	31.3	–	243	82.3	0.8
5	0.51	0.32	2.39	0.214	4044	–	30.7	–	226	80.8	2.1
6	0.60	0.32	2.19	0.276	4045	–	32.8	–	259	80.9	2.6
7	[b, c] 0.78	0.38	3.71	0.210	4246	–	30.6	–	278	81.1	0.5

[a] Best matching giant + star model.
[b] Best matching giant + compact object model.
[c] Best overall model.

Table 8. Properties of the MESA binary models for the giant + star binaries in BPASS that match observations for 2M0412. The initial masses of the stars are listed as M_1 and M_2. The MESA binaries are evolved from an initial orbital period of 25.2 days.

Model	M_1 ($M_\odot$)	M_2 ($M_\odot$)	$M_{\rm giant}$ ($M_\odot$)	$M_{\rm comp}$ ($M_\odot$)	q	$T_{\rm eff,giant}$ (K)	$T_{\rm eff,comp}$ (K)	$R_{\rm giant}$ ($R_\odot$)	$R_{\rm comp}$ ($R_\odot$)	$L_{\rm giant}$ ($L_\odot$)	$L_{\rm comp}$ ($L_\odot$)	$P_{\rm orb}$ (d)	Age Gyr
1	1.60	1.28	0.61	2.27	0.270	4096	11692	29.4	1.6	220	43	81.10	1.7
2	1.40	1.26	0.57	2.09	0.274	4094	10780	28.7	1.7	209	35	81.16	2.6
3	1.60	1.44	0.65	2.39	0.274	4103	11730	30.2	1.8	232	57	81.12	1.7

$1.6 - 1.8\ R_\odot$, $\log(g) \simeq 4.3$ and $L_{\rm comp} \simeq 35 - 57\ L_\odot$. Such a hot companion is grossly incompatible with the NUV limits from *Swift* and *GALEX* (§3.1, Figure 3). This is also significantly hotter than the temperature derived for the second component from fitting the spectra ($T_{\rm eff,comp} = 6347 \pm 700$ K) or the two star `PHOEBE` models ($T_{\rm eff,comp} = 5950^{+170}_{-290}$ K). The key points are that the higher temperatures in the `MESA` models are more consistent with the companion mass and evolutionary state and would also make the companion easily visible.

4.2 Discussion

Table 9 summarizes all of the possible system configurations with single or binary companions comprised of stars, white dwarfs, neutron stars or black holes. We think all binary companions including a star are ruled out by the effect of the orbital motion of the star in the inner binary on the apparent velocity and absorption lines that seem to be associated with the companion. A single WD would be above the Chandrasekhar limit. A single neutron star is also ruled out unless the giant mass can be driven as low as $M_{\rm giant} = 0.45\ M_\odot$ ($R_{\rm giant} \simeq 25\ R_\odot$, Table 6) to allow a $< 2.3\ M_\odot$ neutron star (Raaijmakers et al. 2020). Another problem for either a WD or a NS is that there is likely some accretion and it is not possible for accretion onto these systems to be radiatively inefficient because they have surfaces. A low mass black hole is plausible if the giant's mass is $M_{\rm giant} \gtrsim 0.6 M_\odot$ so that the companion mass can be $\gtrsim 3 M_\odot$. A black hole also allows for accretion with little radiation because the accretion energy can be advected into the black hole rather than being radiated.

Given the luminosity of the giant, single star evolutionary models require high enough masses for the giant, $M_{\rm giant} \simeq 1 M_\odot$ that there is little option other than making a single companion a black hole. However, this is a mass transfer system where our models indicate that the giant is less massive than predicted by single star evolutionary models that match the observed luminosity and effective temperature. A key problem in constraining the giant mass is that ellipsoidal variability really only depends on ratios – mass ratios and radius/semi-major axis ratios – so the mass scale of the system requires an additional dimensional constraint like the radius of the luminous giant. For our previous BH-stellar binary system V723 Mon (Jayasinghe et al. 2021b), the radial velocity residuals analyzed by Masuda & Hirano (2021) break any degeneracy because they provide a constraint on the strength of the ellipsoidal variability with units. If the radius of the giant can be made small enough to allow a low mass giant ($M_{\rm giant} \lesssim 0.4\ M_\odot$, $R_{\rm giant} \lesssim 25\ R_\odot$) with a mass ratio $q \gtrsim 0.3$, and the accreting companion can have a temperature much lower than that predicted by the MESA models, then it is possible for the companion to be a star. In §3.3, we fit `PHOEBE` models to the ZTF r-band and *TESS* light curves at fixed radii. Even at a radius of $R_{\rm giant} = 23\ R_\odot$ ($d \simeq 3.2$ kpc), the mass of the companion is $M_{\rm comp} \simeq 2.1\ M_\odot$. For a stellar companion to remain undetected in the SED, the mass ratio has to be $q > 0.3$, which is inconsistent with all of the `PHOEBE` models in §3.3 and the dynamical measurement from §3.4 (Fig. 8).

For completeness, Table 9 also summarizes the possible double compact object binary companions. A double WD binary can be ruled out because each WD will have a mass that is very close to or exceeds the Chandrasekhar limit. Combining a WD and a NS is allowed, and the NS mass is in the observed range if the WD mass is $> 0.9\ M_\odot$.A double NS binary is feasible. They would need to be of similar mass, since a mass ratio > 0.67 is needed to keep the lower mass NS above the theoretical minimum of $1.2\ M_\odot$ (Suwa et al. 2018). BH plus NS or WD binaries are unlikely as they drive the BH mass further into neutron star territory. A double BH binary seem implausible because they both require BH masses in the range observed for neutron stars. The simplest explanation is again that the dark companion is a mass gap black hole or a high mass neutron star.

Figure 16 shows the masses of black holes discovered through electromagnetic methods, including X-ray binaries and non-interacting systems, as a function of their orbital period. The BH masses and

orbital periods of the X-ray binaries are from Tetarenko et al. (2016). The masses of the non-interacting BHs in the field appear to be lower than expected when compared to the BH mass distribution of the X-ray binaries. A larger sample of non-interacting BHs will be useful to study this mass distribution further.

5 CONCLUSIONS

The evolved red giant 2M04123153+6738486 with $T_{\rm eff,giant} \simeq 4200$ K, $L_{\rm giant} \simeq 230\ L_\odot$ is in a $P = 81.2$ d binary with an unobserved companion. The ASAS-SN, ATLAS, *TESS* and ZTF light curves show that 2M0412 is an ellipsoidal variable (§3.3, Figure 6). The high-resolution Keck/HIRES and LBT/PEPSI spectra indicate that the giant is rapidly rotating (§3.3). `PHOEBE` models of the ellipsoidal variability (§3.3, Table 6) depend on the radius of the giant, which is determined by the distance. For radii of $R_{\rm giant} = 23$ to $33\ R_\odot$, corresponding to distances of $d = 3.2$ to 4.7 kpc, the companion mass is $M_{\rm comp} = 2.1$ to $3.6\ M_\odot$ and the mass of the giant is 0.35 to $0.81\ M_\odot$. The model that is most consistent with the data has $R_{\rm giant} = 29\ R_\odot$ ($d = 4$ kpc), $M_{\rm giant} \simeq 0.60\ M_\odot$, $M_{\rm comp} \simeq 2.98\ M_\odot$, $q \simeq 0.20$ and $i_{\rm orb} \simeq 41.9°$. This best-fitting model is shown as the solid large pentagon in Figure 15. In all the models, the giant is not quite Roche-filling, although it comes close to doing so ($f = R_{\rm giant}/R_{\rm Roche} \simeq 0.90 - 0.97$). The inferred mass of the red giant ($M_{\rm giant} \simeq 0.35 - 0.81\ M_\odot$) is less than expected based on its luminosity and single star evolutionary tracks (§3.1) which implies that the giant has been heavily stripped by binary interaction.

We also detect a secondary component in the spectra (Figure 9) and the RV cross-correlation function (Figure 7), which implies a mass ratio of $q \simeq 0.201 \pm 0.010$ (Figure 8). Simply using this mass ratio leads to companion masses consistent with the `PHOEBE` models. While absorption lines due to accretion disks have previously been observed (Strader et al. 2016), they are very rare. Given that this second component traces the reflex motion expected for a simple binary, it is very unlikely that the companion can itself be a binary.

We can find BPASS binary models very similar to the observed system with both stellar and black hole companions, and in all cases the giant has been partly stripped by mass transfer. MESA models of the cases with a stellar companion, which are needed to properly predict the luminosity and temperature of the companion, predict that a stellar companion would be significantly hotter ($\log T_{\rm eff} \gtrsim 4.0$) and more luminous ($\log(L/L_\odot) \gtrsim 1.5$) than allowed by the observed SED. The observed SED rules out (§3.1, Figure 3) main sequence single (binary) companions more massive than $1.4 M_\odot$ ($2.6 M_\odot$).

We also find a broad, phase variable Hα emission line (§3.5, Figure 11) which is likely due to an accretion disk. The properties of the Hα emission are consistent with Roche lobe overflow from the giant. We derive a *Swift* XRT X-ray flux limit corresponding to $L_{\rm X} \lesssim 3.4 \times 10^{31}$ ergs s^{-1} ($L/L_{\rm edd} \lesssim 10^{-7}$) (§3.6). The simplest explanation for the companion is a single compact object, most likely a black hole, but possibly a high mass neutron star, in the "mass gap" (Table 9, Figure 15).

Assuming the inclination and mass ratio are well-constrained, the only way to have a low mass companion that is sufficiently faint to remain undetected in the SED is by reducing the distance to $d \lesssim 3.5$ kpc while simultaneously increasing the mass ratio to $q \simeq 0.3$ despite the multiple lines of evidence for $q \simeq 0.2$ and a distance of $\simeq 4$ kpc. Deep near-UV observations with the *Hubble* Space Telescope can better constrain the presence of any stellar companion and the nature of any emission from it. Future improvements in *Gaia* parallaxes should remove the ambiguities created by uncertainties in the radius of the giant due to the distance, as would a measurement or constraint on the astrometric orbit (~ 0.1 mas).

ACKNOWLEDGEMENTS

We thank Dr. J. Strader for a careful reading of this manuscript. We thank Dr. J. J. Eldridge for useful discussions on the BPASS models. We thank Dr. Marc Pinsonneault and Lyra Cao for useful discussions. We thank Las Cumbres Observatory and its staff for their continued support of ASAS-SN. ASAS-SN is funded in part by the Gordon and Betty Moore Foundation through grants GBMF5490 and GBMF10501 to the Ohio State University, and also funded in part by the Alfred P. Sloan Foundation grant G-2021-14192.

TJ, KZS and CSK are supported by NSF grants AST-1814440 and AST-1908570. TJ acknowledges support from the Ohio State Presidential Fellowship. TAT is supported in part by NASA grant 80NSSC20K0531. TAT acknowledges previous support from Scialog Scholar grant 24216 from the Research Corporation, from which this effort germinated. J.T.H. is supported by NASA award 80NSSC21K0136. D.H. acknowledges support from the Alfred P. Sloan Foundation, the National Aeronautics and Space Administration (80NSSC18K1585, 80NSSC19K0379), and the National Science Foundation (AST-1717000). CB acknowledges support from the National Science Foundation grant AST-1909022.

Parts of this research were supported by the Australian Research Council Centre of Excellence for All Sky Astrophysics in 3 Dimensions (ASTRO 3D), through project number CE170100013 and the Australian Research Council Centre of Excellence for Gravitational Wave Discovery (OzGrav), through project number CE170100004.

Funding for the Sloan Digital Sky Survey IV has been provided by the Alfred P. Sloan Foundation, the U.S. Department of Energy Office of Science, and the Participating Institutions. SDSS-IV acknowledges support and resources from the Center for High-Performance Computing at the University of Utah. The SDSS web site is www.sdss.org.

SDSS-IV is managed by the Astrophysical Research Consortium for the Participating Institutions of the SDSS Collaboration including the Brazilian Participation Group, the Carnegie Institution for Science, Carnegie Mellon University, the Chilean Participation Group, the French Participation Group, Harvard-Smithsonian Center for Astrophysics, Instituto de Astrofísica de Canarias, The Johns Hopkins University, Kavli Institute for the Physics and Mathematics of the Universe (IPMU) / University of Tokyo, the Korean Participation Group, Lawrence Berkeley National Laboratory, Leibniz Institut für Astrophysik Potsdam (AIP), Max-Planck-Institut für Astronomie (MPIA Heidelberg), Max-Planck-Institut für Astrophysik (MPA Garching), Max-Planck-Institut für Extraterrestrische Physik (MPE), National Astronomical Observatories of China, New Mexico State University, New York University, University of Notre Dame, Observatário Nacional / MCTI, The Ohio State University, Pennsylvania State University, Shanghai Astronomical Observatory, United Kingdom Participation Group, Universidad Nacional Autónoma de México, University of Arizona, University of Colorado Boulder, University of Oxford, University of Portsmouth, University of Utah, University of Virginia, University of Washington, University of Wisconsin, Vanderbilt University, and Yale University.

This work has made use of data from the European Space Agency (ESA) mission *Gaia* (`https://www.cosmos.esa.int/gaia`), processed by the *Gaia* Data Processing and Analysis Consortium. This publication makes use of data products from the Two Micron All Sky Survey, as well as data products from the Wide-field Infrared Survey Explorer. This research was also made possible through the use of

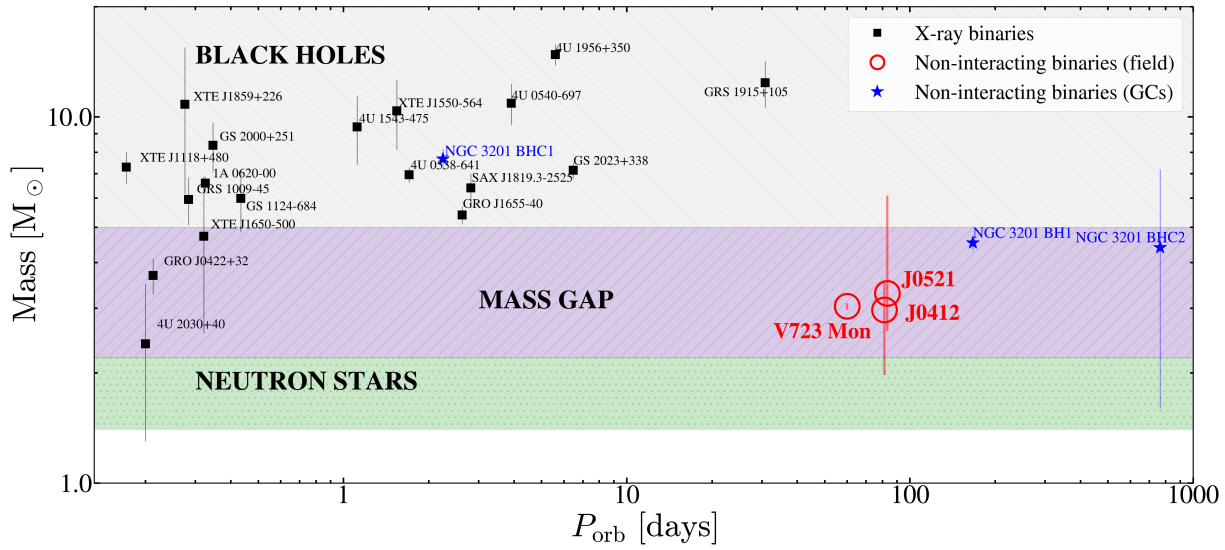

Figure 16. BH masses as a function of orbital period for X-ray binaries (black), non-interacting binaries in globular clusters (blue; Giesers et al. 2018, 2019) and non-interacting binaries in the field (red; Thompson et al. 2019; Jayasinghe et al. 2021b). The BH masses and periods for the X-ray binaries are from Tetarenko et al. (2016). From the limited sample of non-interacting compact objects in the field, we see hints that the typical non-interacting BH masses are lower than expected from the mass distribution of the X-ray binaries.

Table 9. Comparison of the possible scenarios involving stellar companions (*), white dwarfs (WD), neutron stars (NS) and black holes (BH) that can explain the nature of the companion. We assumed $M_{\rm comp} \simeq 3.0\ M_\odot$ from the PHOEBE model with $R_{\rm giant} = 29\ R_\odot$ (§3.3, Table 6). A '✓' indicates that the scenario is possible, a '?' indicates that while the scenario is technically possible, it is very unlikely and a '✗' indicates that the scenario is ruled out. The simplest explanation is that of a single low mass black hole, indicated with '✓✓'.

Dark Companion	Possibility	Comment
Single Star	?	Hot, main sequence companions ruled out by SED limit ($M_* \lesssim 1.4\ M_\odot$).
Single WD	✗	WD will exceed Chandrasekhar limit ($M_{\rm WD} > 1.4\ M_\odot$).
Single NS	✗	NS will exceed maximum mass ($M_{\rm NS} > 2.3\ M_\odot$).
Single BH	✓✓	Simplest explanation.
†Star + Star	✗	Ruled out by SED limit ($M_{\rm binary} \lesssim 2.6\ M_\odot$).
†Star + WD	✗	For $M_* \lesssim 1.4\ M_\odot$, the WD mass exceeds Chandrasekhar limit.
†Star + NS	✗	For $M_* < 1.4\ M_\odot$, the NS mass exceeds $2.2 M_\odot$.
†Star + BH	✗	For $M_* < 1.4\ M_\odot$, the BH mass should be $M_{\rm BH} > 2.8\ M_\odot$.
†WD + WD	✗	Both WD components exceed Chandrasekhar limit.
†NS + WD	✗	NS mass is in the observed range if $M_{\rm WD} > 0.8\ M_\odot$
†BH + WD	✗	BH mass is even lower than with no WD.
†NS + BH	✗	The BH must have a NS-like mass.
†NS + NS	✗	Both NS components should have $M_{\rm NS} \gtrsim 1.2\ M_\odot$, so $q_{\rm inner} \gtrsim 0.67$.
†BH + BH	✗	The BHs have NS masses.

† Disfavored because the orbital motion of an inner binary will dominate over the reflex motion of the giant's orbit observed in our spectra.

the AAVSO Photometric All-Sky Survey (APASS), funded by the Robert Martin Ayers Sciences Fund.

The LBT is an international collaboration among institutions in the United States, Italy and Germany. LBT Corporation partners are: The University of Arizona on behalf of the Arizona Board of Regents; Istituto Nazionale di Astrofisica, Italy; LBT Beteiligungsgesellschaft, Germany, representing the Max-Planck Society, The Leibniz Institute for Astrophysics Potsdam, and Heidelberg University; The Ohio State University, representing OSU, University of Notre Dame, University of Minnesota and University of Virginia.

PEPSI was made possible by funding through the State of Brandenburg (MWFK) and the German Federal Ministry of Educa-

tion and Research (BMBF) through their Verbundforschung grants 05AL2BA1/3 and 05A08BAC.

This research is based on observations made with the *Neil Gehrels Swift Observatory*, obtained from the MAST data archive at the Space Telescope Science Institute, which is operated by the Association of Universities for Research in Astronomy, Inc., under NASA contract NAS 5-26555. This paper includes data collected with the *TESS* mission, obtained from the MAST data archive at the Space Telescope Science Institute (STScI). Funding for the TESS mission is provided by the NASA Explorer Program. STScI is operated by the Association of Universities for Research in Astronomy, Inc., under NASA contract NAS 5-26555.

Some of the data presented herein were obtained at the W. M. Keck Observatory, which is operated as a scientific partnership among the California Institute of Technology, the University of California and the National Aeronautics and Space Administration. The Observatory was made possible by the generous financial support of the W. M. Keck Foundation.

Based on observations obtained with the Samuel Oschin Telescope 48-inch and the 60-inch Telescope at the Palomar Observatory as part of the Zwicky Transient Facility project. ZTF is supported by the National Science Foundation under Grant No. AST-2034437 and a collaboration including Caltech, IPAC, the Weizmann Institute for Science, the Oskar Klein Center at Stockholm University, the University of Maryland, Deutsches Elektronen-Synchrotron and Humboldt University, the TANGO Consortium of Taiwan, the University of Wisconsin at Milwaukee, Trinity College Dublin, Lawrence Livermore National Laboratories, and IN2P3, France. Operations are conducted by COO, IPAC, and UW.

The authors wish to recognize and acknowledge the very significant cultural role and reverence that the summit of Maunakea has always had within the indigenous Hawaiian community. We are most fortunate to have the opportunity to conduct observations from this mountain.

We thank the ZTF and ATLAS projects for making their light curve data publicly available. This research has made use of the VizieR catalogue access tool, CDS, Strasbourg, France. This research also made use of Astropy, a community-developed core Python package for Astronomy (Astropy Collaboration et al. 2013, 2018).

DATA AVAILABILITY

The photometric data are all publicly available. The spectra will be shared on reasonable request to the corresponding author.

REFERENCES

Abbott B. P., et al., 2016, Phys. Rev. Lett., 116, 061102
Abbott B. P., et al., 2017, Phys. Rev. Lett., 119, 161101
Abdul-Masih M., et al., 2020, Nature, 580, E11
Adams S. M., Kochanek C. S., 2015, MNRAS, 452, 2195
Adams S. M., Kochanek C. S., Gerke J. R., Stanek K. Z., Dai X., 2017, MNRAS, 468, 4968
Astropy Collaboration et al., 2013, A&A, 558, A33
Astropy Collaboration et al., 2018, aj, 156, 123
Bailer-Jones C. A. L., Rybizki J., Fouesneau M., Demleitner M., Andrae R., 2021, AJ, 161, 147
Basinger C. M., Kochanek C. S., Adams S. M., Dai X., Stanek K. Z., 2021, MNRAS, 508, 1156
Beech M., 1985, Ap&SS, 117, 69
Bellm E. C., et al., 2019, PASP, 131, 018002
Berger T. A., Huber D., van Saders J. L., Gaidos E., Tayar J., Kraus A. L., 2020, AJ, 159, 280
Bhardwaj A., et al., 2021, ApJ, 909, 200
Bianchi L., Conti A., Shiao B., 2014, Advances in Space Research, 53, 900
Blanco-Cuaresma S., 2019, MNRAS, 486, 2075
Blanco-Cuaresma S., Soubiran C., Heiter U., Jofré P., 2014, A&A, 569, A111
Blanton M. R., et al., 2017, AJ, 154, 28
Bodensteiner J., et al., 2020, A&A, 641, A43
Boothroyd A. I., Sackmann I. J., 1988, ApJ, 328, 641
Bovy J., Rix H.-W., Green G. M., Schlafly E. F., Finkbeiner D. P., 2016, ApJ, 818, 130
Breeveld A. A., et al., 2010, MNRAS, 406, 1687
Bressan A., Marigo P., Girardi L., Salasnich B., Dal Cero C., Rubele S., Nanni A., 2012, MNRAS, 427, 127
Brown G. E., Bethe H. A., 1994, ApJ, 423, 659
Burrows D. N., et al., 2005, Space Sci. Rev., 120, 165
Cardelli J. A., Clayton G. C., Mathis J. S., 1989, ApJ, 345, 245
Castelli F., Kurucz R. L., 2003, in Piskunov N., Weiss W. W., Gray D. F., eds, Vol. 210, Modelling of Stellar Atmospheres. p. A20 (arXiv:astro-ph/0405087)
Chambers K. C., et al., 2016, arXiv e-prints, p. arXiv:1612.05560
Champion D. J., et al., 2008, Science, 320, 1309
Chawla C., Chatterjee S., Breivik K., Krishna Moorthy C., Andrews J. J., Sanderson R. E., 2021, arXiv e-prints, p. arXiv:2110.05979
Chen X., Wang S., Deng L., de Grijs R., Yang M., Tian H., 2020, ApJS, 249, 18
Choi J., Dotter A., Conroy C., Cantiello M., Paxton B., Johnson B. D., 2016, ApJ, 823, 102
Claret A., 2017, A&A, 600, A30
Claret A., Bloemen S., 2011, A&A, 529, A75
Conroy K. E., et al., 2020, ApJS, 250, 34
Dinçer T., Bailyn C. D., Miller-Jones J. C. A., Buxton M., MacDonald R. K. D., 2018, ApJ, 852, 4
Dixon D., Tayar J., Stassun K. G., 2020, AJ, 160, 12
Dotter A., 2016, ApJS, 222, 8
Drimmel R., Cabrera-Lavers A., López-Corredoira M., 2003, A&A, 409, 205
Eggleton P. P., 1983, ApJ, 268, 368
El-Badry K., Burdge K., 2021, arXiv e-prints, p. arXiv:2111.07925
El-Badry K., Quataert E., 2020a, arXiv e-prints, p. arXiv:2006.11974
El-Badry K., Quataert E., 2020b, MNRAS, 493, L22
El-Badry K., Burdge K. B., Mróz P., 2021, arXiv e-prints, p. arXiv:2112.05030
Eldridge J. J., Stanway E. R., 2016, MNRAS, 462, 3302
Eldridge J. J., Stanway E. R., Xiao L., McClelland L. A. S., Taylor G., Ng M., Greis S. M. L., Bray J. C., 2017, Publ. Astron. Soc. Australia, 34, e058
Elitzur M., Ivezić Ž., 2001, MNRAS, 327, 403
Farr W. M., Sravan N., Cantrell A., Kreidberg L., Bailyn C. D., Mandel I., Kalogera V., 2011, ApJ, 741, 103
Fender R. P., Russell D. M., Knigge C., Soria R., Hynes R. I., Goad M., 2009, MNRAS, 393, 1608
Foreman-Mackey D., Hogg D. W., Lang D., Goodman J., 2013, PASP, 125, 306
Gagné J., et al., 2018, ApJ, 856, 23
Gaia Collaboration Brown A. G. A., Vallenari A., Prusti T., de Bruijne J. H. J., Babusiaux C., Biermann M., 2020, arXiv e-prints, p. arXiv:2012.01533
Giesers B., et al., 2018, MNRAS, 475, L15
Giesers B., et al., 2019, A&A, 632, A3
Gray R. O., Corbally C. J., 1994, AJ, 107, 742
Green G. M., Schlafly E., Zucker C., Speagle J. S., Finkbeiner D., 2019, ApJ, 887, 93
Groenewegen M. A. T., 2021, A&A, 654, A20
Gunn J. E., et al., 2006, AJ, 131, 2332
Gustafsson B., Edvardsson B., Eriksson K., Jørgensen U. G., Nordlund Å., Plez B., 2008, A&A, 486, 951
HI4PI Collaboration et al., 2016, A&A, 594, A116
Heinze A. N., et al., 2018, AJ, 156, 241
Henden A. A., Levine S., Terrell D., Welch D. L., Munari U., Kloppenborg B. K., 2018, in American Astronomical Society Meeting Abstracts #232.

p. 223.06
Hogg D. W., Eilers A.-C., Rix H.-W., 2019, AJ, 158, 147
Horvat M., Conroy K. E., Pablo H., Hambleton K. M., Kochoska A., Giammarco J., Prša A., 2018, ApJS, 237, 26
Howard A. W., et al., 2010, ApJ, 721, 1467
Huber D., et al., 2017, ApJ, 844, 102
Hynes R. I., Robinson E. L., Bitner M., 2005, ApJ, 630, 405
Irrgang A., Geier S., Kreuzer S., Pelisoli I., Heber U., 2020, A&A, 633, L5
Ivezic Z., Elitzur M., 1997, MNRAS, 287, 799
Jayasinghe T., et al., 2018, MNRAS, 477, 3145
Jayasinghe T., et al., 2021a, MNRAS, 503, 200
Jayasinghe T., et al., 2021b, MNRAS, 504, 2577
Kochanek C. S., 2020, MNRAS, 493, 4945
Kochanek C. S., et al., 2017, PASP, 129, 104502
Kolb U., Ritter H., 1990, A&A, 236, 385
Kolbl R., Marcy G. W., Isaacson H., Howard A. W., 2015, AJ, 149, 18
Lennon D. J., Dufton P. L., Villaseñor J. I., Evans C. J., Langer N., Saxton R., Monageng I. M., Toonen S., 2021, arXiv e-prints, p. arXiv:2111.12173
Lenz P., Breger M., 2005, Communications in Asteroseismology, 146, 53
Lindegren L., et al., 2021a, A&A, 649, A2
Lindegren L., et al., 2021b, A&A, 649, A2
Liu Q. Z., van Paradijs J., van den Heuvel E. P. J., 2006, A&A, 455, 1165
Liu J., et al., 2019, Nature, 575, 618
Marshall D. J., Robin A. C., Reylé C., Schultheis M., Picaud S., 2006, A&A, 453, 635
Martin D. V., et al., 2019, A&A, 624, A68
Masci F. J., et al., 2019, PASP, 131, 018003
Masuda K., Hirano T., 2021, ApJ, 910, L17
Mazzola Daher C., et al., 2021, arXiv e-prints, p. arXiv:2110.01100
McDonald I., Zijlstra A. A., 2015, MNRAS, 448, 502
Morris S. L., 1985, ApJ, 295, 143
Morrissey P., et al., 2007, ApJS, 173, 682
Mortier A., et al., 2016, A&A, 585, A135
Narayan R., Yi I., 1995, ApJ, 452, 710
Orosz J. A., Hauschildt P. H., 2000, A&A, 364, 265
Orosz J. A., Bailyn C. D., Remillard R. A., McClintock J. E., Foltz C. B., 1994, ApJ, 436, 848
Özel F., Psaltis D., Narayan R., McClintock J. E., 2010, ApJ, 725, 1918
Paczynski B., 1977, ApJ, 216, 822
Patton R. A., Sukhbold T., Eldridge J. J., 2021, arXiv e-prints, p. arXiv:2106.05978
Paxton B., Bildsten L., Dotter A., Herwig F., Lesaffre P., Timmes F., 2011, ApJS, 192, 3
Paxton B., et al., 2013, ApJS, 208, 4
Paxton B., et al., 2015, ApJS, 220, 15
Paxton B., et al., 2018, ApJS, 234, 34
Paxton B., et al., 2019, ApJS, 243, 10
Pejcha O., Thompson T. A., 2015, ApJ, 801, 90
Petigura E. A., 2015, PhD thesis, University of California, Berkeley
Poole T. S., et al., 2008, MNRAS, 383, 627
Price-Whelan A. M., Goodman J., 2018, ApJ, 867, 5
Price-Whelan A. M., Hogg D. W., Foreman-Mackey D., Rix H.-W., 2017, ApJ, 837, 20
Prša A., et al., 2016, ApJS, 227, 29
Raaijmakers G., et al., 2020, ApJ, 893, L21
Ramírez I., Allende Prieto C., Lambert D. L., 2013, ApJ, 764, 78
Reimers D., 1975, Memoires of the Societe Royale des Sciences de Liege, 8, 369
Ricker G. R., et al., 2015, Journal of Astronomical Telescopes, Instruments, and Systems, 1, 014003
Rivinius T., Baade D., Hadrava P., Heida M., Klement R., 2020, A&A, 637, L3
Roming P. W. A., et al., 2005, Space Sci. Rev., 120, 95
Rowan D. M., Stanek K. Z., Jayasinghe T., Kochanek C. S., Thompson T. A., Shappee B. J., Holoien T. W. S., Prieto J. L., 2021, MNRAS, 507, 104
Saracino S., et al., 2021, arXiv e-prints, p. arXiv:2111.06506
Schönrich R., Binney J., Dehnen W., 2010, MNRAS, 403, 1829
Ségransan D., et al., 2011, A&A, 535, A54
Shao Y., Li X.-D., 2019, ApJ, 885, 151
Shappee B. J., et al., 2014, ApJ, 788, 48
Shenar T., et al., 2020, A&A, 639, L6
Skrutskie M. F., et al., 2006, AJ, 131, 1163
Smak J., 1981, Acta Astron., 31, 395
Stanway E. R., Eldridge J. J., 2018, MNRAS, 479, 75
Stevance H., Eldridge J., Stanway E., 2020, The Journal of Open Source Software, 5, 1987
Strader J., et al., 2015, ApJ, 804, L12
Strader J., Li K.-L., Chomiuk L., Heinke C. O., Udalski A., Peacock M., Shishkovsky L., Tremou E., 2016, ApJ, 831, 89
Straizys V., Kuriliene G., 1981, Ap&SS, 80, 353
Strassmeier K. G., et al., 2015, Astronomische Nachrichten, 336, 324
Strassmeier K. G., Ilyin I., Steffen M., 2018, A&A, 612, A44
Sukhbold T., Ertl T., Woosley S. E., Brown J. M., Janka H. T., 2016, ApJ, 821, 38
Suwa Y., Yoshida T., Shibata M., Umeda H., Takahashi K., 2018, MNRAS, 481, 3305
Tayar J., et al., 2015, ApJ, 807, 82
Ter Braak C. J. F., 2006, Statistics and Computing, 16, 239
Tetarenko B. E., Sivakoff G. R., Heinke C. O., Gladstone J. C., 2016, ApJS, 222, 15
The LIGO Scientific Collaboration et al., 2021, arXiv e-prints, p. arXiv:2111.03606
Thompson T. A., et al., 2019, Science, 366, 637
Tonry J. L., et al., 2018, PASP, 130, 064505
Torres M. A. P., Casares J., Martínez-Pais I. G., Charles P. A., 2002, MNRAS, 334, 233
Trimble V. L., Thorne K. S., 1969, ApJ, 156, 1013
Vallely P. J., Kochanek C. S., Stanek K. Z., Fausnaugh M., Shappee B. J., 2020, arXiv e-prints, p. arXiv:2010.06596
Verbunt F., Phinney E. S., 1995, A&A, 296, 709
Vogt S. S., et al., 1994, in Crawford D. L., Craine E. R., eds, Society of Photo-Optical Instrumentation Engineers (SPIE) Conference Series Vol. 2198, Instrumentation in Astronomy VIII. p. 362, doi:10.1117/12.176725
Wade R. A., Horne K., 1988, ApJ, 324, 411
Wilson J. C., et al., 2019, PASP, 131, 055001
Woosley S. E., Sukhbold T., Janka H. T., 2020, ApJ, 896, 56
Wright E. L., et al., 2010, AJ, 140, 1868
Wu J., et al., 2015, ApJ, 806, 92
Zheng L.-L., et al., 2019, AJ, 158, 179
Zinn J. C., 2021, AJ, 161, 214
van Belle G. T., et al., 1999, AJ, 117, 521

This paper has been typeset from a TEX/LATEX file prepared by the author.